Structural and Multidisciplinary Optimization (2018) 58:2431–2454
https://doi.org/10.1007/s00158-018-2117-x

RESEARCH PAPER

Topology optimisation of biphasic adsorbent beds for gas storage

R. C. R. Amigo[1,2] · D. S. Prado[1] · J. L. Paiva[1] · R. W. Hewson[2] · E. C. N. Silva[1]

Received: 11 June 2018 / Revised: 19 August 2018 / Accepted: 19 September 2018 / Published online: 27 October 2018
© The Author(s) 2018

Abstract
Adsorption is a retention mechanism of fluid molecules on solid surfaces and presents a wide range of applications, such as fuel storage, refrigeration and separation processes. This work describes the modelling of gas adsorption on porous media and presents an optimisation approach for the design of adsorption systems based on biphasic adsorbent beds by topology optimisation. A comprehensive formulation for the adsorption phenomenon is presented, detailing the derivation of governing equations and respective weak forms and discretisation for the implementation of the finite element method (FEM). A new topology optimisation material model based on offset hyperbolic tangents is introduced. The derivation of sensitivities is presented in detail, based on a transient adjoint problem. A diverse set of optimised adsorbed natural gas (ANG) tanks, considering real material properties of activated carbon and steel, is presented. Results indicate the suitability of the method in optimising the distribution of phases across adsorbent beds and show that biphasic ANG tanks can perform significantly better than traditional tanks.

Keywords Topology optimisation · Finite element method · Adsorption · Gas storage · Heat transfer

1 Introduction

The flow of gases or liquids in porous media are subjected to the retention and release of molecules on the solid phase. One of the retention mechanisms is the sorption phenomenon, which is a general term adopted for both adsorption and absorption reactions. The former is a surface reaction in which gas moleculesaccumulate on the surface of solid particles attracted by disrupted bonds (Mota et al. 2004), while the latter is a bulk phenomenon, in which gas molecules diffuse through another phase, accumulating at the grain boundaries and often forming a new phase (Blanco et al. 2014).

Adsorption is divided into two categories: (i) physical adsorption, based on weak van der Waals forces, which is also know as physisorption and (ii) chemical adsorption, based on covalent bondings, also know as chemisorption. While the former is easily reversible and leaves the adsorbent intact, the latter involves a chemical reaction that affect the surfaces, as is the case of corrosion phenomenon. Figure 1 illustrates the mechanism of adsorption, where molecules concentrate on micro-pores walls.

The capacity of adsorption of porous media is dependent on characteristics such as the distribution and characteristic of micropores on the adsorbent and the affinity of adsorbent and adsorbate (Biloė et al. 2002). The capacity of adsorption is also directly proportional to the pressure and inversely proportional to the temperature. During an adsorption cycle, the adsorbent bed temperature naturally tends to increase, since the adsorption reaction is exothermic, releasing heat when a molecule of gas is adsorbed by the surface. Conversely, the desorption reaction is endothermic, consuming heat when molecules detaches from the surface. Therefore, the major challenge in designing adsorption systems is often the internal temperature variation, which

Responsible Editor: YoonYoung Kim

✉ R. C. R. Amigo
rcr13@imperial.ac.uk

D. S. Prado
pradodis@usp.br

J. L. Paiva
jolpaiva@usp.br

R. W. Hewson
r.hewson@imperial.ac.uk

E. C. N. Silva
ecnsilva@usp.br

[1] Escola Politecnica, University of Sao Paulo, Sao Paulo, Brazil

[2] Imperial College London, London, UK

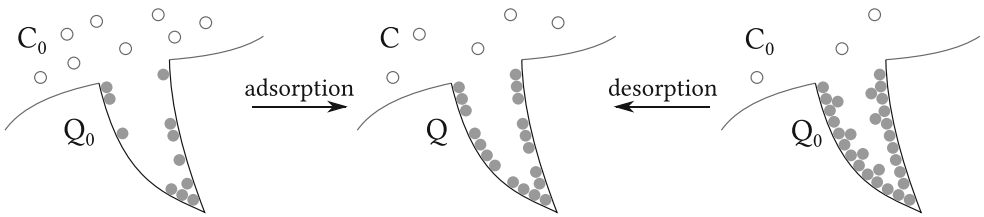


Fig. 1 Distribution of molecules in gaseous (○) and adsorbed (●) phases

prevents the system to reach its full capacity of gas adsorption and hinders the adsorbent bed purge.

Several engineering applications are based on the adsorption process, such as fluid separation, refrigeration, CO_2 capture and storage (CCS) and gas fuel storage. In the case of natural gas storage, adsorbed natural gas (ANG) tanks consist of a solid matrix of activated carbon (AC) with natural gas molecules accumulated in its pores. Due to the relatively high density of the adsorbed phase, an overall storage capacity around 164 *V*/*V* (164 times denser than at atmospheric temperature and pressure) can be achieved at room temperature with pressure ranging from 35 to 50 atm (Hirata et al. 2009). Conversely, compressed natural gas (CNG) is ordinarily stored at 200 atm, offering a capacity of 245 *V*/*V*. In turn, liquefied natural gas (LNG) requires cryogenic temperatures to force gas condensation, which happens, for methane, around 113 K and provides a storage capacity of 600 *V*/*V* (Hirata et al. 2009). These characteristics place ANG as a promising method to maintain gas confinement, as it works at atmospheric temperature and much lower pressure than CNG.

A common objective when designing ANG tanks is to maximise the mass of gas that can be stored and recovered in reasonable short adsorption and desorption cycles. Such tanks require materials presenting high capacity of adsorption and appropriate thermal management. The amount of gas a bed is able to adsorb is determined by its microstructure. Activated carbons presenting the highest adsorption of natural gas typically have narrow microporosity and micropores width of 2.0 nm (Biloė et al. 2002). Monte Carlo simulations determined that the theoretical maximum capacity of adsorption for methane is 209 *V*/*V* on monolithic carbon and 146 *V*/*V* on pelletised carbon (Matranga et al. 1992). It has been shown that, due to the temperature variation, real discharge cycles in ANG tanks may present between 8 and 29% loss of capacity when compared to ideal isothermal cycles (Chang and Talu 1996). Thermal management can be addressed by varying the tank shape and boundary conditions. Different flow rates, aspect ratios and convection coefficients can increase significantly the storage capacity of cylindrical tanks when imposing forced convection on relatively slim tanks (Sahoo et al. 2011). Adsorption of hydrogen on activated carbon has been improved about 25% by inserting equally distributed metallic fins on an adsorbent bed connected to a cold source at 233 K (Vasiliev et al. 2014). Active cooling has also been used to improve ANG tanks performance, through the addition of cooling jackets (Mota et al. 2004) and fin-tube type heat exchangers (Rahman et al. 2011).

The use of topology optimisation on the design of adsorption systems has not been reported in literature, although key concepts can be inherited from heat transfer and fluid problems. Topology optimisation has been applied to heat transfer problems for many years. Cases include the cross-section optimisation of a minimum-material fin (Anagnostou et al. 1992), material optimisation in transient heat conduction problems (Turteltaub 2001), electrothermal microactuators subjected to top heat convection (Sigmund 2001) and convection-dominated problems (Bruns 2007). The application to fluid systems is introduced by the design of channels seeking the minimisation of power dissipation (Borrvall and Petersson 2003), which has been extended to incompressible laminar viscous flow at moderate Reynolds numbers (Gersborg-Hansen et al. 2005) and generalised for scaled for Stokes and Darcy equations (Guest and Prėvost 2006). The use of topology optimisation in problems coupling heat transfer and fluids is also reported, as in the optimisation of heat dissipating structures with forced convection (Yoon 2010; Koga et al. 2013; Matsumori et al. 2013; Kontoleontos et al. 2012) and in the design of optimised electro-thermo-mechanical (ETM) actuators by considering their interaction with the surrounding fluid (Yoon 2012). A detailed review of topology optimisation applied to heat transfer and fluid flow systems is presented in Dbouk (2017).

The objective of this work is to design optimised ANG tanks by distributing non-adsorbent materials across the adsorbent bed, as demonstrated in the tank depicted in Fig. 2, to achieve high storage densities faster than full-carbon tanks. Given the complexity of adsorption systems, such design problem is approached by topology optimisation. The objective function is the maximisation of gas intake during a filling cycle of fixed length. The transition between adsorbent and non-adsorbent materials is made through an offset hyperbolic tangent material model. Resulting topologies are based on the optimisation of two-dimensional domains, representing axisymmetric or very long tanks.

This paper is organised as follows. In Section 2, the theoretical modelling of adsorption systems is presented.

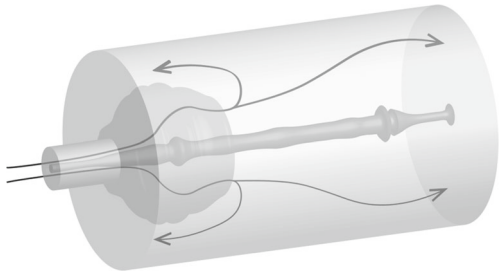


Fig. 2 Optimisation of ANG tanks through the addition of non-adsorbent materials

In Section 3, the optimisation problem is defined with respective material models and objective functions. In Section 4, the numerical implementation of the adsorption model and sensitivities are presented. Optimised topologies are presented and discussed in Section 5. Concluding remarks are presented in Section 6.

2 Modelling of adsorption systems

A typical adsorption domain Ω is illustrated in Fig. 3, where Γ_W and Γ_L denote sub-regions from $\partial\Omega$ where boundary conditions of wall and gas inlet/outlet are imposed, respectively.

In this work, the following assumptions are made:

Ideal gases: in the systems considered, gases are considered to present ideal thermodynamic behaviour (Sahoo et al. 2011), therefore, their densities are described by:

$$\rho_g = \frac{M_g P}{R_g T} \tag{1}$$

where M_g is the molar gas mass, R_g is the universal gas constant, P is the gas pressure and T is the gas temperature.

Darcy's Porous media: the Darcy's law governs the fluid flow through porous media, making the velocity to be given by:

$$\mathbf{v}_g = -\frac{K_s}{\mu_g}\nabla P \tag{2}$$

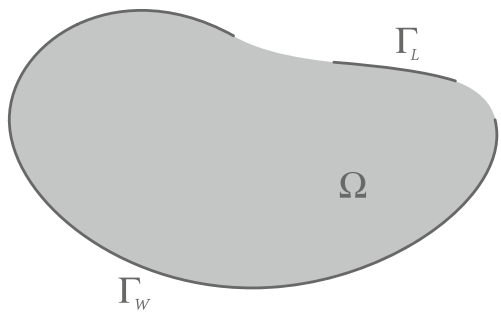


Fig. 3 Adsorption domain

Local thermal equilibrium: the adsorbent bed is locally in thermal equilibrium with the gas (Mota et al. 2004). All intra-particle and film resistances in heat and mass transfer are neglected.

Constant specific heat capacity: the specific heat capacity is considered to be constant within the typical range of temperatures observed in adsorption systems. Its variation is neglected since it usually varies around only 8% (Mota et al. 2004) in a range of $100K$.

Constant adsorption enthalpy: this work considers an approximation in which ΔH assumes a constant mean value within the range of pressures and temperatures studied (Sahoo et al. 2011).

Lagergren adsorption model: For the studied cases, it is considered that the film diffusion is dominant and the rate of adsorption is governed by Lagergren model (Vasiliev et al. 2014).

2.1 Dependency of material properties on porosities

Effective properties of porous media are dependent on macro-porosity (ε_M) and microporosity (ε_m). Given these two classes of porosity, the total porosity (ε_t) is defined as:

$$\varepsilon_t = \varepsilon_M + (1-\varepsilon_M)\varepsilon_m \tag{3}$$

Density: it is given by the sum of gaseous and solid phase weighted by the total porosity, ε_t, with the addition of the density of adsorbed gas, Q, which is considered to occupy a neglectful volume:

$$\rho_f(\varepsilon_t) = \varepsilon_t\rho_g + (1-\varepsilon_t)\rho_s + Q \tag{4}$$

Permeability: dependent on the macro-porosity, following the Kozeny-Carman's model for spherical particles (Carman 1937):

$$K_s(\varepsilon_M) = \frac{\phi_s^2\varepsilon_M^3}{72\tau_s(1-\varepsilon_M)^2} \tag{5}$$

where ϕ_s is the effective characteristic particle diameter and τ_s denotes the pores tortuosity.

Thermal conductivity: it can be given by both Maxwell-Eucken's or Russel's relations (Smith et al. 2013). The former considers the effect of large spherical pores with thin walls and the latter the effect of a cubic pore inclusion in the material matrix by considering a parallel/series resistor. Here, the conductivity of the thin film of gas adsorbed, k_q, is neglected and the Maxwell-Eucken relation is adopted to

interpolate the gaseous and solid conductivities (Smith et al. 2013):

$$k_f(\varepsilon_t) = k_s \frac{k_g + 2k_s + 2\varepsilon_t(k_g - k_s)}{k_g + 2k_s - \varepsilon_t(k_g - k_s)} \tag{6}$$

where k_s and k_g are the thermal conductivities for the solid and gas, respectively.

2.2 Adsorption and desorption kinetics

The concentration q represents the mass of adsorbed phase per mass of adsorbent. Therefore, the density of adsorbed phase in reference to the volume of the adsorbent bed, Q, is given by:

$$Q = (1 - \varepsilon_t)\rho_s q \tag{7}$$

The specific volume of micropores, w_s, represents the volume of micropores per mass of adsorbent. The ratio of micropores volume per adsorbent bed volume, W_s, is then given by:

$$W_s = (1 - \varepsilon_t)\rho_s w_s \tag{8}$$

From the equilibrium concentration of adsorbed gas, q_{eq} (Sahoo et al. 2011), the equilibrium density of adsorbed gas is given by:

$$Q_{eq} = \rho_{adg} W_s \, exp\left(-\left(\frac{A}{\beta E_0}\right)^{n_f}\right) \tag{9}$$

where β is the affinity coefficient of the adsorbent-adsorbate pair, E_0 is the characteristic energy of adsorption and n_s stands for the effective micro-pores dispersion.

The local adsorbed gas density, ρ_{adg}, is given by Sahoo et al. (2011):

$$\rho_{adg} = \frac{\rho_{boil}}{exp(\alpha_e(T - T_{boil}))} \tag{10}$$

where ρ_{boil} is the gas density at boiling point temperature (T_{boil}) and α_e is the mean value of the thermal expansion of liquefied gases.

The Polanyi's adsorption potential, A, is given by:

$$A = R_g T ln\left(\frac{P_{sat}}{P}\right) \tag{11}$$

which saturated pressure P_{sat} is given by:

$$P_{sat} = P_{cr}\left(\frac{T}{T_{cr}}\right)^2 \tag{12}$$

where P_{cr} and T_{cr} are, respectively, the critical pressure and temperature of the gas.

The rate of adsorption decreases as more gas is adsorbed, following the LDF model given by the following expression (Mota et al. 1996):

$$\begin{aligned} \frac{\partial Q}{\partial t} &= G(Q_{eq} - Q) \;\; in \; \Omega \times [0, t_f] \\ Q &= Q_{ini} \;\; in \; \Omega \; at \; t = 0 \end{aligned} \tag{13}$$

where the coefficient G, which dictates the adsorption and desorption kinetics, is given by Vasiliev et al. (2012):

$$G = D \, exp\left(\frac{-E_{[a,d]}}{R_g T}\right) \tag{14}$$

where the activation energy of adsorption (E_a) is considered when $Q \leq Q_{eq}$ and the activation energy of desorption (E_d) otherwise. D is the intra-particle diffusional time constant, given by Sahoo et al. (2011):

$$D = 4\frac{D_0}{\phi_s^2} \tag{15}$$

where ϕ_s is the characteristic particle diameter and D_0 is the gas diffusivity.

2.3 Continuity

In adsorption systems, the coupled continuity equations of gaseous, solid and adsorbed phases is expressed by Sahoo et al. (2011):

$$\frac{\partial}{\partial t}\left(\varepsilon_t \rho_g + (1 - \varepsilon_t)\rho_s + Q\right) + \nabla \cdot \left(\rho_g \mathbf{v}_g\right) = 0 \tag{16}$$

where Q is the mass of adsorbed gas per unit of adsorbent volume and ρ_s is the bulk adsorbent density, which is constant.

By substituting the ideal gas and Darcy's laws, the balance becomes:

$$\frac{\varepsilon_t M_g}{R_g}\frac{\partial}{\partial t}\left(\frac{P}{T}\right) + \frac{\partial Q}{\partial t} - \frac{M_g}{R_g \mu_g}\nabla \cdot \left(K_s \frac{P}{T}\nabla P\right) = 0 \tag{17}$$

where the solid density ρ_s is considered constant.

A pressure inlet condition is imposed on Γ_L, representing the connection of the tank to an infinite reservoir at fixed pressure and temperature or the opening of the tank to the atmosphere. Inlet pressure is varied smoothly, being approximated by the following sinusoidal profile:

$$P_{\Gamma_L} = \begin{cases} P_{ini} + sin^2\left(\frac{\pi}{2}\frac{t}{\sigma t_f}\right)(P_{let} - P_{ini}) & , t < \sigma t_f \\ P_{let} & , t \geq \sigma t_f \end{cases} \tag{18}$$

where P_{ini} and P_{let} denote initial and filling/emptying pressures, t_f is the final time and σ is a smoothness factor. Figure 4 illustrates P_{Γ_L} curves for the adsorption cycle.

2.4 Energy balance

The energy balance of the gaseous phase is given in terms of Cp_g and T as Bird et al. (2007):

$$\begin{aligned} &\frac{\partial \rho_g Cp_g T}{\partial t} + \nabla \cdot (\rho_g Cp_g T \mathbf{v}_g) - \nabla \cdot (k_g \nabla T) \\ &+ \boldsymbol{\tau} : \nabla \mathbf{v}_g - \left.\frac{\partial ln V}{\partial ln T}\right|_P \frac{DP}{Dt} - \rho_g T \frac{DCp_g}{Dt} = 0 \end{aligned} \tag{19}$$



Fig. 4 Inlet pressure (P_{Γ_L}) during adsorption cycle

where the specific heat capacity, Cp_g, is considered constant, $\boldsymbol{\tau}$ denotes the viscous stress tensor, $\frac{\partial lnV}{\partial lnT} = 1$ for ideal gases and D denotes the Lagrangian derivative.

Following the assumptions of negligible viscous dissipation and Darcy's porous media flow, the energy balance becomes:

$$\rho_g Cp_g \frac{\partial T}{\partial t} + Cp_g T \left\{ \frac{\partial \rho_g}{\partial t} + \nabla \cdot (\rho_g \mathbf{v}_g) \right\}_{\mathcal{C}} - \rho_g Cp_g \frac{K_s}{\mu_g} \nabla P \cdot \nabla T - \nabla \cdot (k_g \nabla T) - \frac{\partial P}{\partial t} + \left\{ \frac{K_s}{\mu_g} \nabla P \cdot \nabla P \right\}_{\approx 0} = 0 \tag{20}$$

where the continuity equation is observed in $\mathcal{C}$, making these terms to vanish, and the last term is neglected, given the very small pressure gradients observed in the range of permeabilities of interest in this work.

Analogously, the energy balance of the solid and adsorbed phases are given by:

$$\rho_s Cp_s \frac{\partial T}{\partial t} - \nabla \cdot (k_s \nabla T) = 0 \tag{21}$$

$$Q Cp_q \frac{\partial T}{\partial t} - \nabla \cdot (k_q \nabla T) = |\Delta H| \frac{\partial Q}{\partial t} \tag{22}$$

where ΔH denotes the isosteric heat of adsorption.

The energy balance for coupled gaseous, solid and adsorbed phases assuming local thermal equilibrium between phases (Mota et al. 2004) and ideal gas is then given by the following expression:

$$\varepsilon_t \left(\frac{Cp_g M_g}{R_g} \frac{P}{T} \frac{\partial T}{\partial t} - \frac{\partial P}{\partial t} \right) + (1 - \varepsilon_t) \left(\rho_s Cp_s \frac{\partial T}{\partial t} \right) + Cp_g Q \frac{\partial T}{\partial t} - \frac{Cp_g M_g}{R_g \mu_g} K_s \frac{P}{T} \nabla P \cdot \nabla T - \nabla \cdot \left(k_f \nabla T \right) = |\Delta H| \frac{\partial Q}{\partial t} \tag{23}$$

where the effective thermal conductivity, k_f, is given by (6).

Inlet heat flux is considered on Γ_L, which is expressed by the following Robin boundary condition (Sahoo et al. 2011):

$$-k_f \frac{\partial T}{\partial \mathbf{n}} = \frac{M_g Cp_g K_s}{R_g \mu_g} \frac{P}{T} \nabla P \cdot \mathbf{n} \, (T - T_{let}) \tag{24}$$

Assuming that heat convection takes place on the walls, a Robin boundary condition is defined on Γ_W:

$$-k_f \frac{\partial T}{\partial \mathbf{n}} = h_W (T - T_\infty) \tag{25}$$

On the region $\Gamma \setminus (\Gamma_W \cup \Gamma_L)$, since no boundary terms are explicitly defined, the heat flux is null, representing adiabatic condition.

3 Topology optimisation of ANG tanks

Figure 5 illustrates the typical variation of the average gas density, temperature and pressure in an ANG tank used as an on-demand source of fuel, such as in gas-powered vehicles or in residences. Starting from the average density of total gas at the equilibrium, $\overline{(Q + \rho_g)_{ini,a}}$, the tank admits gas while pressure and temperature increase during the filling cycle, reaching the final average total density of $\overline{(Q + \rho_g)_{fin,a}}$. Such average density is conserved inside the tank until its future depletion. While the tank is kept quiescent, its temperature slowly approaches the equilibrium with the atmospheric temperature, T_{atm}, causing its internal pressure to drop due to the gas phase change from gaseous to adsorbed. The stored gas is then delivered through a nearly isothermal desorption, maintaining equilibrium with T_{atm} during the whole emptying cycle.

The goal when designing ANG tanks applied to on-demand consumption is to maximise the total intake of gas during the filling cycle by mitigating the rise of the adsorbent bed temperature. A possible approach to improve heat transfer is not to occupy the full volume of the tank

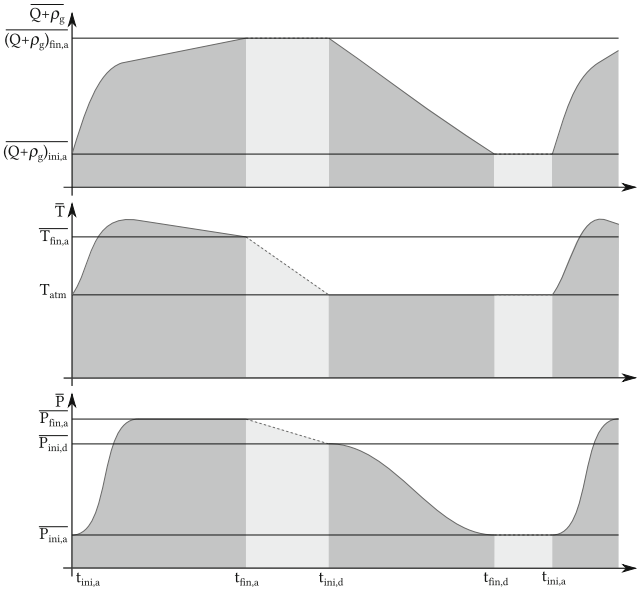


Fig. 5 Typical cycle of ANG tanks applied to on-demand consumption

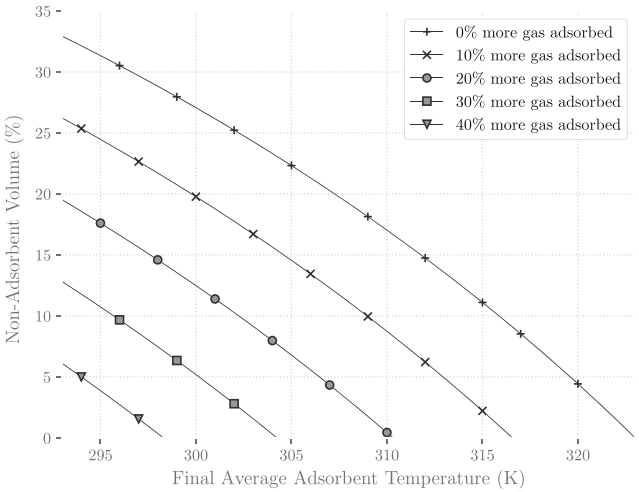


Fig. 6 Isomassic curves given by the variation of adsorbent temperature and percentage of volume occupied by non-adsorbent material

with adsorbent, replacing it by other materials, presenting interesting thermal properties, in suitable regions.

However, the temperature reduction must be enough to compensate the lost of adsorbent material volume. Figure 6 illustrates such trade-off for a tank presenting the final average temperature of 323 K at the end of the adsorption cycle. It is shown how much volume is possible to occupy with non-adsorbent materials according to the reduction of the temperature in order to achieve certain gain in the mass of gas adsorbed. For instance, if the final average temperature of tank is 293 K, the same mass of gas could be adsorbed using only 67% of the original adsorbent volume. By using 80% of the original volume, it would be possible to increase the total amount of gas adsorbed in 20%.

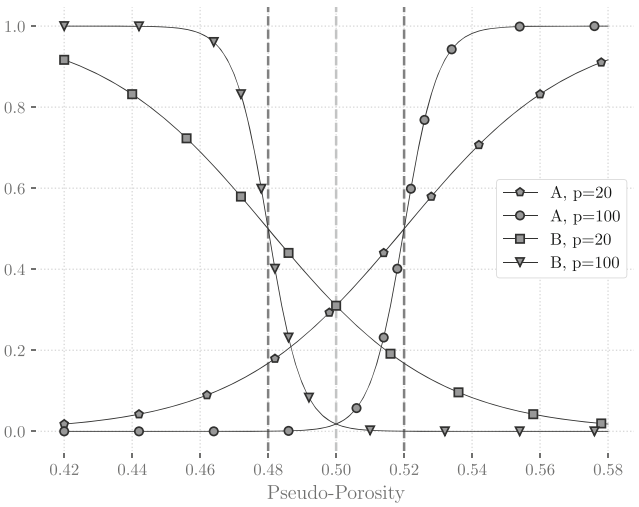


Fig. 7 Material model for properties A and B with $\epsilon = 0.02$

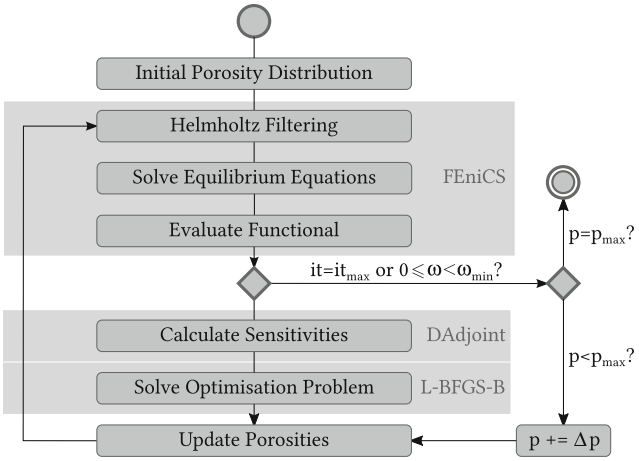


Fig. 8 Optimisation algorithm flowchart

Topology optimisation is adopted to find optimised distributions of non-adsorbent material across the adsorbent bed. The alternation between adsorbent (ads) and non-adsorbent (non) materials in the domain is expressed by the pseudo-porosity e as follows:

$$\Pi(\mathrm{e}) = \begin{cases} \Pi_{non}, & \text{if } \mathrm{e} = 0 \\ \Pi_{ads}, & \text{if } \mathrm{e} = 1 \end{cases} \tag{26}$$

where the actual property $\Pi(\mathrm{e})$ is given by Π_{ads} or Π_{non} depending on e value.

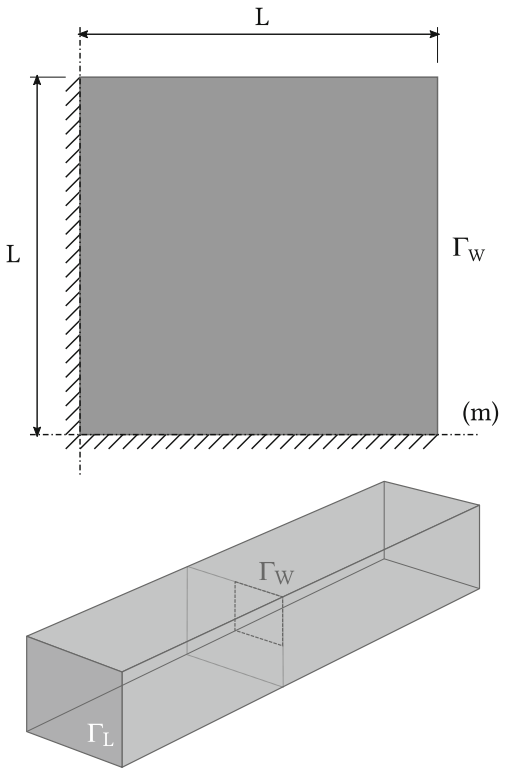


Fig. 9 Prismatic domain

Table 1 Optimisation parameters for prismatic tank

Domain	
Dimensions:	$L = 0.25$ m
Materials:	Appendix C
Heat convection:	$h_{\Gamma_W} = 100$ W/m.K
Cycle	
Temperatures:	$T_{ini,\infty} = 293$ K
Initial pressure:	$P_{ini} = 0.1$ MPa
Final pressure:	$P_{let} = 1.0$ MPa
Smoothness:	$\sigma = 0.1$, (18)
Time length:	$t_{f,a} = 10\,800$ s, Fig. 5
FEM	
Mesh elements:	31 999 (simplex)
Mesh cell diameter:	2.50×10^{-3} m
Timestep:	$\Delta t = 10$ s
TOM	
Objective:	Gas intake J_a, (30)
Initial guess:	$\mathbf{e} = \mathbf{0.5}$
Material model:	$\epsilon = 0.02$
	$p_{ini} = 1$
	$p_{fin} = 51$
	$\Delta p = 5$, (28)
Filter radius:	$z = 5.0 \times 10^{-3}$ m, (29)
Max iterations per step:	$it_{max} = 20$
Tolerance:	$\omega_{min} = 1.0 \times -6$

However, such binary law of material defines an ill-posed problem, with multiple local minima (Bendsøe and Sigmund 1999). Such issue can be avoided by relaxing the definition and assuming intermediate values, ranging from 0 to 1. Since only 0 and 1 represent existent materials, it is desirable to recover the discrete nature of this material law.

In the optimisation of biphasic adsorbent beds, intermediate materials often constitute the best solution from the optimiser perspective. For instance, in the case of seeking an optimised placement of steel on a carbon bed, the conductivity of the non-adsorbent material is usually more than 200 times larger than adsorbent's and steel adsorption capacity is null. Therefore, a material presenting half of steel conductivity and half of carbon adsorption capacity is a good solution, although it is not a real material.

Table 2 Total gas intake in homogeneous and optimised prismatic tanks

	Gas intake (J_a)
Homogenous tank:	1.16 kg
Optimised tank:	1.23 kg
Improvement:	6.03%

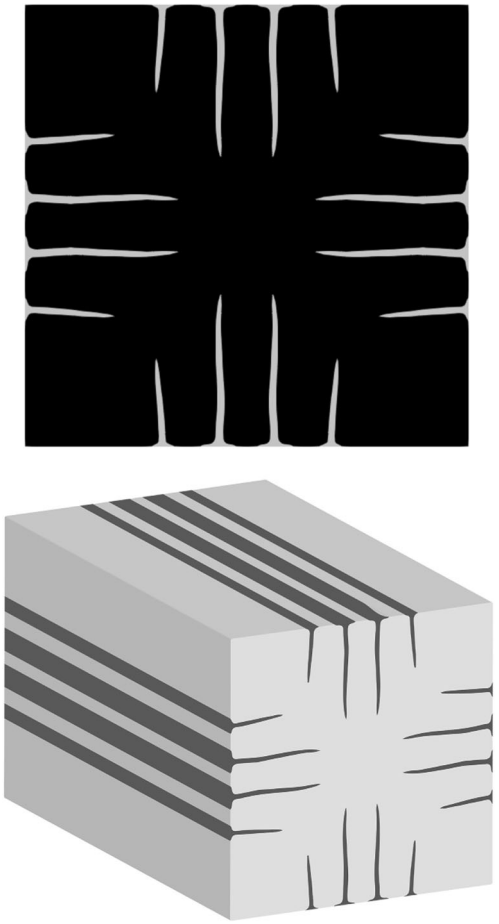


Fig. 10 Optimised prismatic tank section

It is then necessary to adopt a material model which forces the optimiser to clearly choose one or other material. The material model based on offset hyperbolic tangents

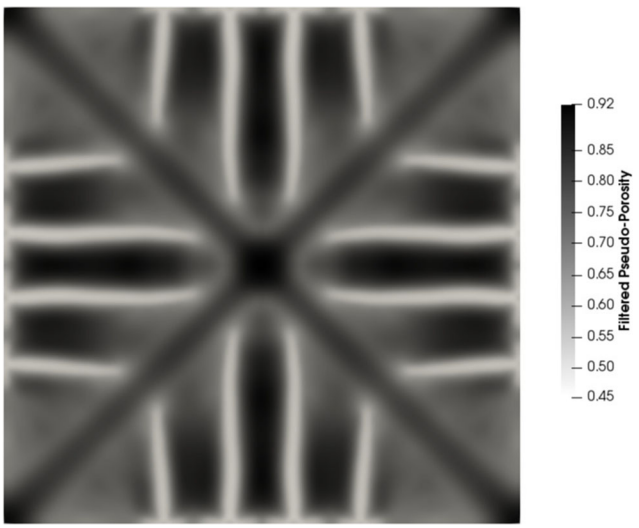


Fig. 11 Filtered pseudo-porosity distribution in optimised prismatic tank section

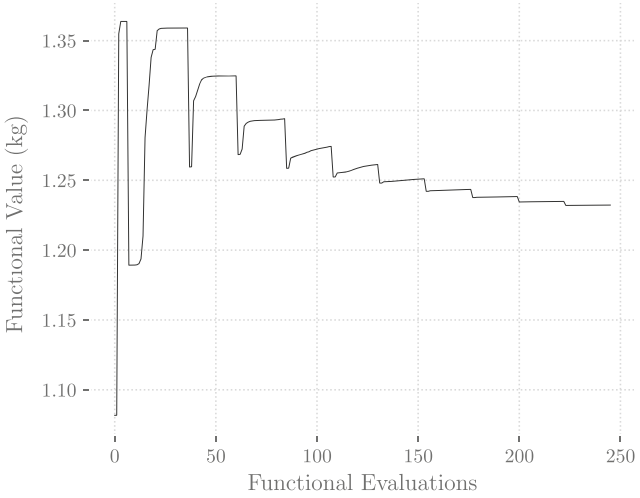


Fig. 12 Objective function convergence in the prismatic tank optimisation

presented in (27) is suitable for this sort of necessity. For the property Π_A, where the functional of interest $J(\Pi_{A,ads})$ (adsorbent property in the whole domain) is higher than $J(\Pi_{A,non})$ (non-adsorbent property in the whole domain), the phase change is centred on $\mathrm{e}_c = 0.5 + \epsilon$. Conversely, for a property Π_B which presents $J(\Pi_{B,non})$ higher than $J(\Pi_{B,ads})$, $\mathrm{e}_c = 0.5 - \epsilon$ is adopted. In the absence of an offset, there would be intermediate properties at $\mathrm{e} = 0.5$ regardless of the penalisation value. Figure 7 illustrates such material model for the offset $\epsilon = 0.02$.

$$\Pi(\mathrm{e}) = (1 - m(\mathrm{e}))\,\Pi_{non} + m(\mathrm{e})\Pi_{ads} \tag{27}$$

where:

$$m(\mathrm{e}) = \frac{\tanh\left[p\,(\mathrm{e} + \mathrm{sgn}\,(J(\Pi_{non}) - J(\Pi_{ads}))\,\epsilon - 0.5)\right] + 1}{2} \tag{28}$$

with sgn denoting the signum function.

Topology optimisation presents inherent issues such as checker-board instability and mesh dependency, which are mitigated in this work by filtering the design variables before inputting them to the material model based on the solution of the following Helmholtz-type PDE (Lazarov and Sigmund 2011):

$$-z^2\nabla^2\mathrm{e} + \mathrm{e} = \phi \tag{29}$$

where the distribution ϕ is smoothed to the C^2 function e, according to the filter length parameter z.

The final optimisation problem for the design of ANG tanks for on-demand consumption is expressed as:

$$\begin{aligned} \text{Maximise}: \; & J_a(\phi) = \left[\int_\Omega \left(Q(\mathrm{e}) + \rho_g(\mathrm{e})\right)\, dx\right]_{t_{ia}}^{t_{fa}} \\ \text{subjected to}: \; & 0 \le \phi \le 1 \\ & \text{Eq. (17)} - \text{Continuity} \\ & \text{Eq. (23)} - \text{Energy Balance} \\ & \text{Eq. (13)} - \text{Adsorption Kinetics} \\ & \text{Eq. (29)} - \text{Helmholtz Filtering} \end{aligned} \tag{30}$$

4 Numerical implementation

Modelling and optimisation of adsorption systems are implemented in this work aided by FEniCS (Logg 2007), its module Dolfin-Adjoint (Funke and Farrell 2015) and Scipy's L-BFGS-B optimiser (Byrd et al. 1995; Jones et al. 2011). The numerical formulation of such implementation is presented in this section.

4.1 Adsorption problem

The solution of the adsorption governing equations is approximated via finite element method (FEM). In order to do so, the inner product of the strong PDEs and arbitrary test

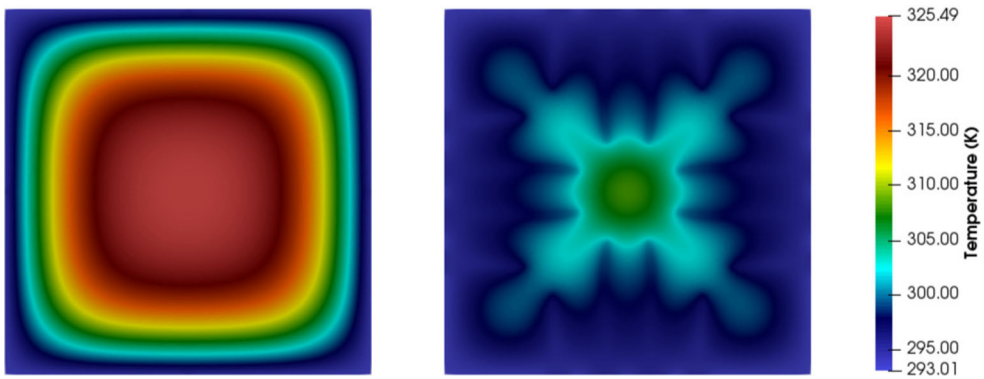


Fig. 13 Temperature distribution in homogeneous (left) and optimised prismatic (right) tanks sections at the end of the adsorption cycle

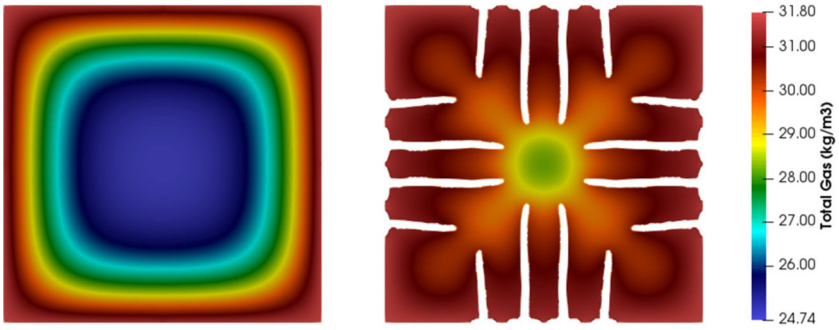


Fig. 14 Total gas distribution in homogeneous (left) and optimised prismatic (right) tanks sections at the end of the adsorption cycle

functions is integrated on the problem domain originating a weak formulation which is satisfied numerically. This procedure is detailed in Appendix A.1 and results in the following set of discrete non-linear equations:

$$\begin{aligned}\mathbf{M_{tp}(T)}\,\dot{\mathbf{P}} + \mathbf{M_{tt}(P,T)}\,\dot{\mathbf{T}} + \mathbf{M_{tq}}\,\dot{\mathbf{Q}} + \mathbf{M_{sp}(P,T)}\,\mathbf{P} &= \mathbf{0}\\ \mathbf{E_{tp}}\,\dot{\mathbf{P}} + \mathbf{E_{tt}(P,T,Q)}\,\dot{\mathbf{T}} + \mathbf{E_{tq}}\,\dot{\mathbf{Q}} + \mathbf{E_{st}(P,T)}\,\mathbf{T} &= \mathbf{0}\\ \mathbf{D_{tq}}\,\dot{\mathbf{Q}} + \mathbf{D_{sq}(T)}\mathbf{Q} &= \mathbf{D_r(P,T)}\end{aligned} \tag{31}$$

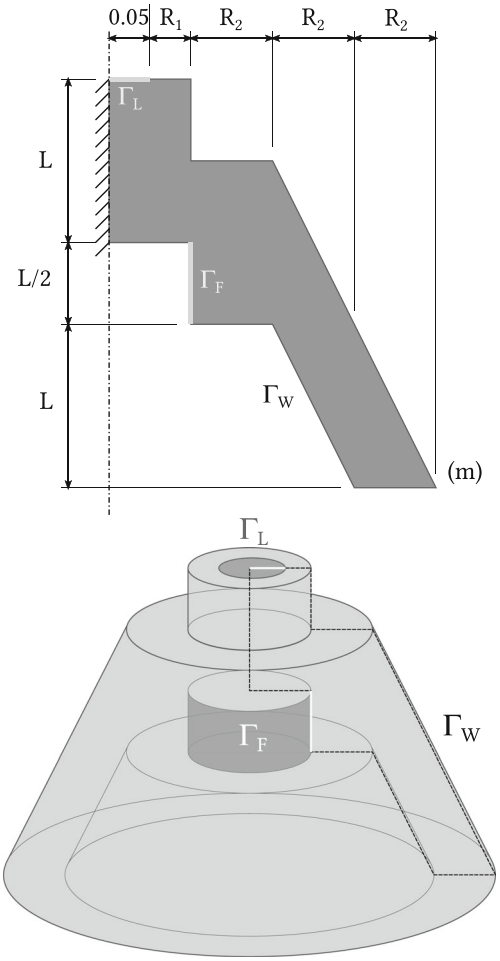


Fig. 15 Complex axisymmetric domain

originating the following system:

$$\begin{bmatrix}\mathbf{M_{tp}(T)} & \mathbf{M_{tt}(P,T)} & \mathbf{M_{tq}}\\ \mathbf{E_{tp}} & \mathbf{E_{tt}(P,T,Q)} & \mathbf{E_{tq}}\\ \mathbf{0} & \mathbf{0} & \mathbf{D_{tq}}\end{bmatrix}\begin{Bmatrix}\dot{\mathbf{P}}\\ \dot{\mathbf{T}}\\ \dot{\mathbf{Q}}\end{Bmatrix} + \begin{bmatrix}\mathbf{M_{sp}(P,T)} & \mathbf{0} & \mathbf{0}\\ \mathbf{0} & \mathbf{E_{st}(P,T)} & \mathbf{0}\\ \mathbf{0} & \mathbf{0} & \mathbf{D_{sq}(T)}\end{bmatrix}\begin{Bmatrix}\mathbf{P}\\ \mathbf{T}\\ \mathbf{Q}\end{Bmatrix} = \begin{Bmatrix}\mathbf{0}\\ \mathbf{0}\\ \mathbf{D_r(P,T)}\end{Bmatrix} \tag{32}$$

Table 3 Optimisation parameters for complex axisymmetric tank

Domain	
Dimensions:	$R_2 = 0.1$ m, $L = 0.2$ m
Materials:	Appendix C
Heat convection:	$h_{\Gamma_W} = 5$ W/m.K
Cold finger:	$T_{\Gamma_F} = 273$ K
Cycle	
Temperature:	$T_{ini,let,\infty} = 293$ K
Initial pressure:	$P_{ini} = 0.1$ MPa
Final pressure:	$P_{let} = 1.0$ MPa
Smoothness:	$\sigma = 0.1$, (18)
Time length:	$t_{fin,a} = 3\,600$ s, Fig. 5
FEM	
Mesh elements:	34 211 (simplex)
Mesh cell diameter:	1.632×10^{-3} m (min)
Timestep:	$\Delta t = 10$ s
TOM	
Objective:	Gas intake J_a, (30)
Initial guess:	$\mathbf{e} = \mathbf{0.5}$
Material model:	$\epsilon = 0.02$
	$p_{ini} = 1$
	$p_{fin} = 51$
	$\Delta p = 5$, (28)
Filter radius:	$z = 5.0 \times 10^{-3}$ m, (29)
Max iterations per step:	$it_{max} = 20$
Tolerance:	$\omega_{min} = 1.0 \times -6$

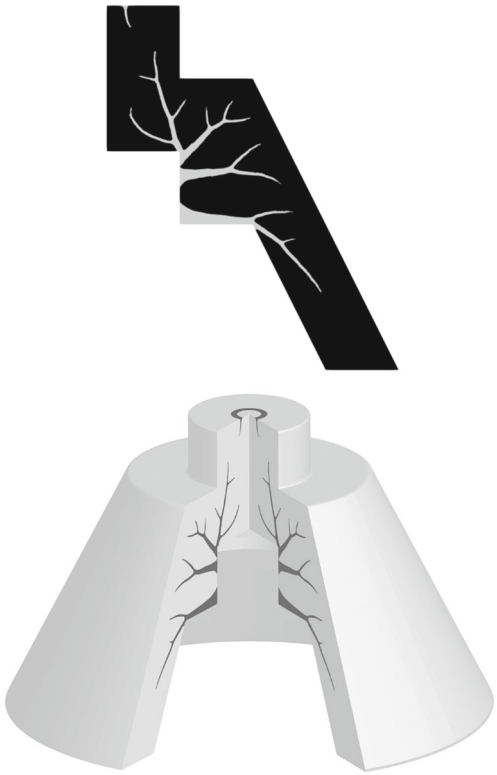


Fig. 16 Optimised complex axisymmetric tank

which is rewritten as:

$$\mathbf{F}_t(\mathbf{w})\dot{\mathbf{w}} + \mathbf{F}_s(\mathbf{w})\mathbf{w} = \mathbf{F}_r(\mathbf{w}) \tag{33}$$

where the state variable $\mathbf{w}$ is constituted by pressure, temperature and adsorbed gas:

$$\mathbf{w} = \begin{Bmatrix} \mathbf{P} \\ \mathbf{T} \\ \mathbf{Q} \end{Bmatrix} \tag{34}$$

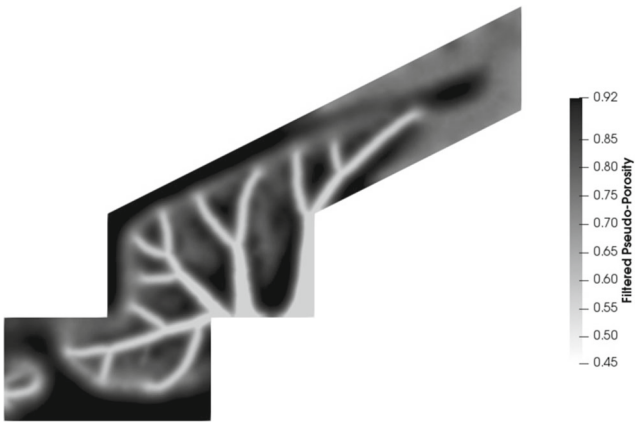


Fig. 17 Filtered pseudo-porosity distribution in optimised complex axisymmetric tank section

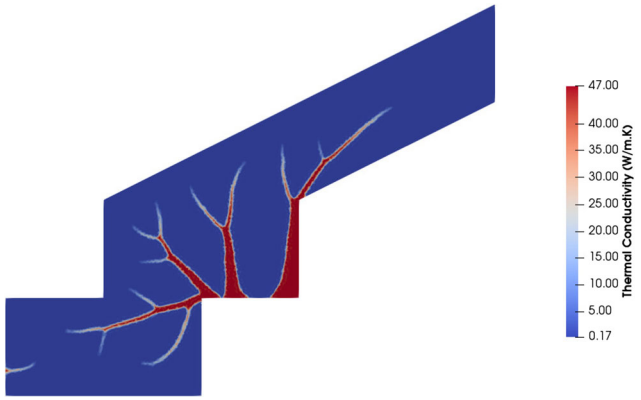


Fig. 18 Thermal conductivity in optimised complex axisymmetric tank section

Based on implicit Euler method for time discretisation, the n-th timestep of such system is given by:

$$\mathbf{F}_t(\mathbf{w}_n)\frac{\mathbf{w}_n - \mathbf{w}_{n-1}}{\Delta t} + \mathbf{F}_s(\mathbf{w}_n)\mathbf{w}_n = \mathbf{F}_r(\mathbf{w}_n) \tag{35}$$

The following lower-triangular system is then defined:

$$\mathbf{C}\begin{Bmatrix} \mathbf{w}_0 \\ \mathbf{w}_1 \\ \vdots \\ \mathbf{w}_{N-1} \\ \mathbf{w}_N \end{Bmatrix} = \begin{Bmatrix} \mathbf{w}_{ia} \\ \mathbf{F}_r(\mathbf{w}_1) \\ \vdots \\ \mathbf{F}_r(\mathbf{w}_{N-1}) \\ \mathbf{F}_r(\mathbf{w}_N) \end{Bmatrix} \tag{36}$$

where $\mathbf{w}_{ia}$ denotes the initial state conditions and the matrix $\mathbf{C}$ is given by:

$$\mathbf{C} = \begin{bmatrix} \mathbf{I} & \mathbf{0} & \cdots & \mathbf{0} & \mathbf{0} \\ \mathbf{C}_P(\mathbf{w}_0) & \mathbf{C}_C(\mathbf{w}_1) & \cdots & \mathbf{0} & \mathbf{0} \\ \vdots & \vdots & \ddots & \vdots & \vdots \\ \mathbf{0} & \mathbf{0} & \cdots & \mathbf{C}_P(\mathbf{w}_{N-1}) & \mathbf{C}_C(\mathbf{w}_N) \end{bmatrix} \tag{37}$$

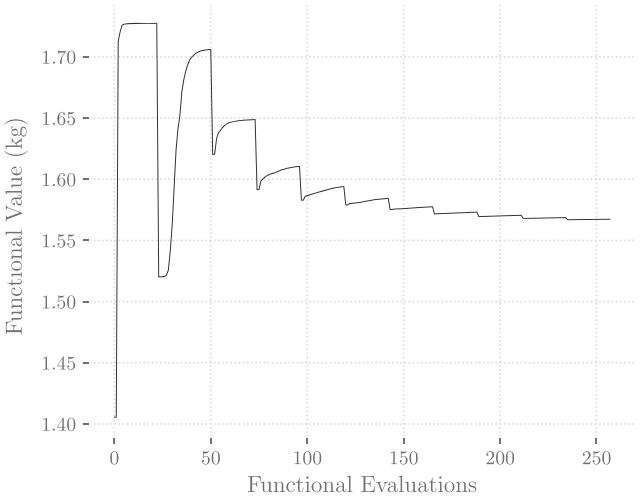


Fig. 19 Objective function convergence in the complex axisymmetric tank optimisation

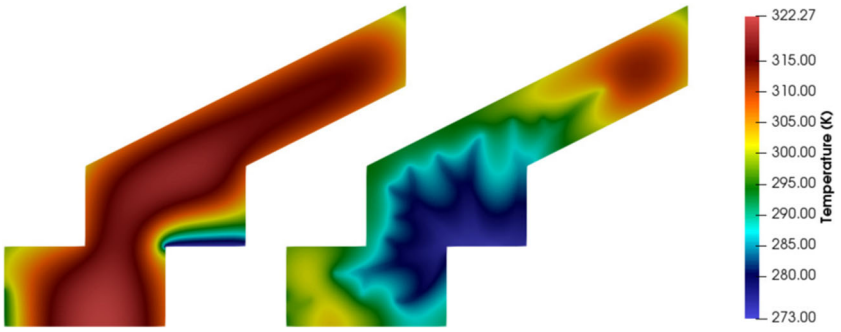


Fig. 20 Temperature distribution in homogeneous (left) and optimised complex axisymmetric (right) tanks sections at the end of the adsorption cycle

where:

$$\mathbf{C}_P(\mathbf{w}_n) = -\frac{\mathbf{F}_t(\mathbf{w}_n)}{\Delta t} \tag{38}$$

$$\mathbf{C}_C(\mathbf{w}_n) = \frac{\mathbf{F}_t(\mathbf{w}_n)}{\Delta t} + \mathbf{F}_s(\mathbf{w}_n) \tag{39}$$

4.2 Sensitivities calculation

The sensitivity of the functional J_a in respect to the design variable e_j is obtained via adjoint method, which is described in detail in Appendix A.3. The final sensitivity expression is given by:

$$\frac{dJ_a}{d\mathrm{e}_j} = \int_{t_{ia}}^{t_{fa}} \left[\left(\delta_{t_{fa}} - \delta_{t_{ia}}\right) \frac{\partial B}{\partial \mathrm{e}_j} + \boldsymbol{\lambda}^T \left(\frac{\partial \mathbf{F}_t}{\partial \mathrm{e}_j} \dot{\mathbf{w}} + \frac{\partial \mathbf{F}_s}{\partial \mathrm{e}_j} \mathbf{w} - \frac{\partial \mathbf{F}_r}{\partial \mathrm{e}_j} \right) \right] dt - \boldsymbol{\lambda}^T \mathbf{F}_t \frac{d\mathbf{w}}{d\mathrm{e}_j}\bigg|_{t_{ia}} \tag{40}$$

where δ denotes the Dirac's delta (centred on time instants t_{fa} and t_{ia}), $\boldsymbol{\lambda}$ is the adjoint variable and B is the total gas mass, which is defined in Appendix A.3 by (75).

Despite the functional and PDE systems being expressed in terms of filtered pseudo-densities, e_j, the optimisation is based on non-filtered pseudo-densities, ϕ_j.

The discrete Helmholtz filtering system is given by:

$$\mathbf{Z}\boldsymbol{\phi} = \boldsymbol{\phi} \tag{41}$$

where $\mathbf{Z}$ and $\boldsymbol{\phi}$ are defined in Appendix A.2.

The implicit derivative of such system in respect to ϕ_j results in:

$$\frac{d\mathbf{Z}}{d\phi_j}\mathbf{e} + \mathbf{Z}\frac{d\mathbf{e}}{d\phi_j} = \frac{d\boldsymbol{\phi}}{d\phi_j} \tag{42}$$

where the first term is null, given that $\mathbf{Z}$ is not dependent on pseudo-porosities, and the right-hand side is:

$$\frac{d\boldsymbol{\phi}}{d\phi_j} = \boldsymbol{\delta}_{jk} \tag{43}$$

in which $\boldsymbol{\delta}_{jk}$ denotes the Kronecker's delta column vector, being null in all lines, except for the j-th, which is equal to 1.

The sensitivity of the functional J to the non-filtered pseudo-porosity ϕ_j is then given by:

$$\frac{dJ}{d\phi_j} = \left(\frac{dJ}{d\mathbf{e}}\right)^T \frac{d\mathbf{e}}{d\phi_j} = \left(\frac{dJ}{d\mathbf{e}}\right)^T \mathbf{Z}^{-1}\boldsymbol{\delta}_{jk} \tag{44}$$

4.3 Optimisation algorithm

The optimisation algorithm follows the flow represented in Fig. 8. In the optimisation loop, the sensitivities are obtained

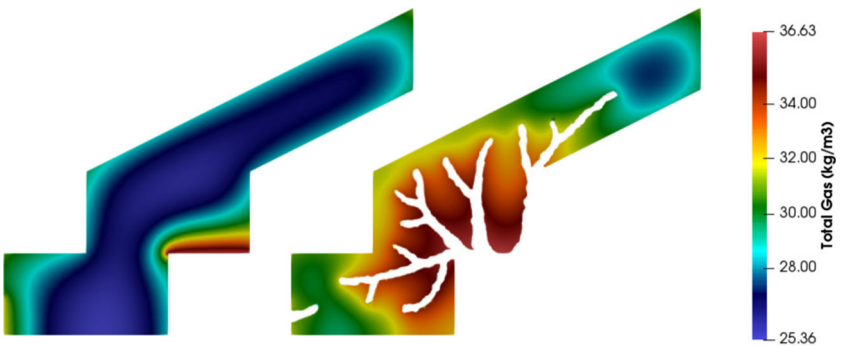


Fig. 21 Total gas distribution in homogeneous (left) and optimised complex axisymmetric (right) tanks sections at the end of the adsorption cycle

Table 4 Total gas intake in homogeneous and optimised complex axisymmetric tanks

	Gas intake (J_a)
Homogenous tank:	1.42 kg
Optimised tank:	1.56 kg
Improvement:	9.86%

via dolfin-adjoint based on the equilibrium equations solved on FEniCS. The optimiser L-BFGS-B (Byrd et al. 1995; Jones et al. 2011) receives the sensitivities and output a new distribution of design variables, aiming to improve the functional of interest. The relative functional variation is defined by considering the last two iterations:

$$\omega = \frac{J_{it} - \frac{J_{it-1}+J_{it-2}}{2}}{\frac{J_{it-1}+J_{it-2}}{2}} \tag{45}$$

When the functional relative variation is non-negative and smaller than a tolerance ω_{min} or when the maximum number of iterations it_{max} is reached, the loop is broken. The penalisation p is then increased by Δp, following the continuation method, and the loop is restarted. This algorithm is performed until reaching the maximum penalisation p_{max}, when the final topology is defined.

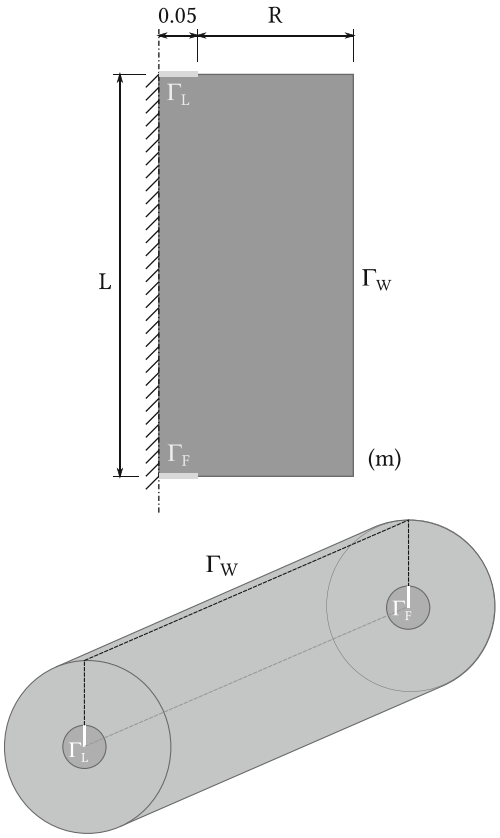


Fig. 22 Cylindrical domain

5 Results and discussion

This section presents examples of the method implemented on a set of different tanks constituted by activated carbon subjected to methane adsorption.

5.1 Prismatic tanks

A two-dimensional reduction of a three-dimensional prismatic tank is presented in Fig. 9. It consists on the approximation of a very long tank with fixed cross-section. Based on symmetry, only one quarter of such section is considered. In this domain, the impact of the gas inlet is not present and the pressure is constant on the whole section, making the convective term in the energy balance null. In this and following examples, the adsorbent bed is considered to be wrapped by a thin sheet of metallic material subject to heat exchange with the room through convection. The

Table 5 Optimisation parameters for cylindrical tank

Domain	
Dimensions:	$L = 1.0$ m, $R = 0.15$ m
Materials:	Appendix C
	$Cp_{non} = 1880$ J/kg.K
Heat convection:	$h_{(\Gamma_W \cup \Gamma_F)} = 5$ W/m.K
Cycle	
Temperatures:	$T_{ini,let,\infty} = 293$ K
Initial pressure:	$P_{ini} = 0.1$ MPa
Final pressure:	$P_{let} = 1.0$ MPa
Smoothness:	$\sigma = 0.1$, (18)
Time length:	$t_{f,a} = 3\,600$ s, Fig. (5)
FEM	
Mesh elements:	31 999 (simplex)
Mesh cell diameter:	2.50×10^{-3} m
Timestep:	$\Delta t = 10$ s
TOM	
Objective:	Gas intake J_a, (30)
Initial guess:	$\mathbf{e} = \mathbf{0.5}$
Material model:	$\epsilon = 0.02$
	$p_{ini} = 20$
	$p_{fin} = 100$
	$\Delta p = 10$, (28)
Filter radius:	$z = 5.0 \times 10^{-3}$ m, (29)
Max iterations per step:	$it_{max} = 10$
Tolerance:	$\omega_{min} = 1.0 \times -6$

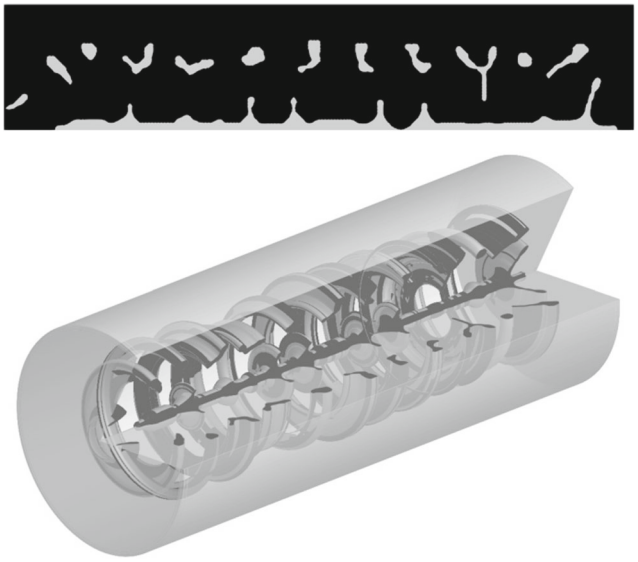


Fig. 23 Optimised cylindrical tank with high thermal capacity material

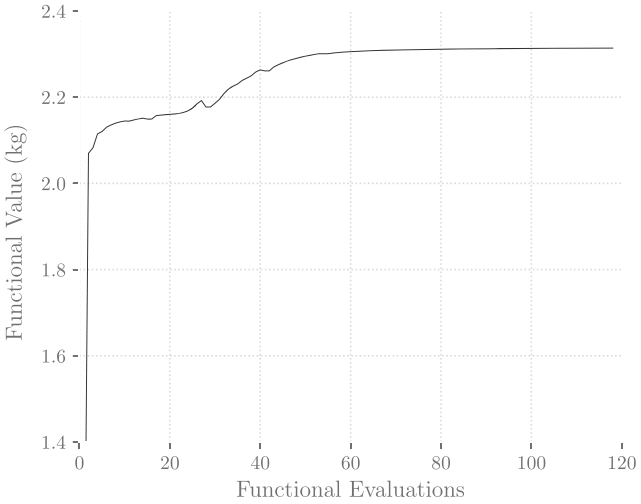


Fig. 25 Objective function convergence in the cylindrical tank with high heat capacity material optimisation

contribution of this wall to the energy balance is assumed to be neglectful (Sahoo et al. 2011) and it is not included in the model. In fact, being a thin sheet, its Biot number (Bi) is very small and the heat conduction inside it is much faster than the heat convection away from its surface.

TOM implementation is based on the parameters shown in Table 1. It consists of a square section 0.5 m wide subjected to forced convection of 100 W/m.K. The adsorption cycle lasts 10 800 s (3 h), in which the pressure is smoothly increased during the first 1 800 s from 0.1 to 1.0 MPa. The material model defined in (28) with an offset $\epsilon = 0.02$. The optimisation procedure is based on L-BFGS-B optimiser and starts with the homogeneous distribution of the design variables values at $\mathbf{e} = 0.5$. The penalisation is smoothly increasing from $p_{ini} = 1$ to $p_{fin} = 51$, following the continuation method limited to a maximum of 20 iterations per continuation step (Table 1).

The resulting topology depicted in Fig. 10 shows perfectly symmetric steel fins connecting the central region of the section to the walls subjected to forced convection. The threshold defining the transition from activated carbon to steel is set on $e = 0.5$. As seen in Fig. 11, the material model adopted makes such interface clearly defined. The convergence of the objective function is shown in Fig. 12. Figure 13 shows that the fins made the maximum temperature inside the domain drop from 325 to 310 K, allowing 6.03% more gas to be admitted during the filling cycle (Table 2), despite the adsorbent volume lost (Fig. 14).

5.2 Complex axisymmetric tanks

An axisymmetric domain based on the radial section shown in Fig. 15 is considered to demonstrate the implementation of the method to complex shaped tanks. Walls on Γ_W are subjected to natural convection ($h = 5$ W/m.K) while a fixed temperature of 273 K is imposed to the region denoted by Γ_F. The full description of the model parameters is presented in Table 3.

The resulting optimised topology is seen in Fig. 16. Metallic limbs occur mainly in the vicinity of the cold wall Γ_F, but also around the inlet region Γ_L. Such distribution

Fig. 24 Filtered pseudo-porosity distribution in optimised cylindrical tank with high heat capacity material section



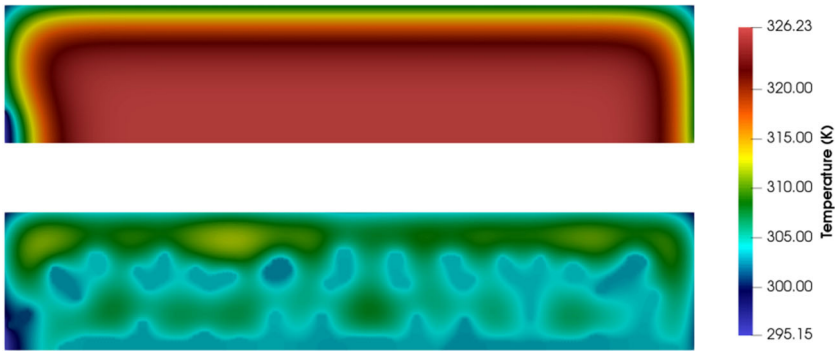


Fig. 26 Temperature distribution in homogeneous (top) and optimised cylindrical (bottom) tanks with high heat capacity material sections at the end of the adsorption cycle

allows the spreading of the lower temperatures of these regions to the inside of the domain. Even before the thresholding at e $=$ 0.5, the metallic limbs contours are very clear, as seen in Fig. 17. Due to the material model adopted, grey regions seen in the topology do not represent intermediate materials, as demonstrated by the effective thermal conductivity plotted in Fig. 18. The convergence of the objective function is shown in Fig. 19.

The strategy adopted by the optimisation algorithm is to grow metallic limbs across regions with high temperature gradient. Figure 20 shows a reduction of the central zone temperature, which increases the density of gas as observed in Fig. 21. Such strategy leads to an improvement of 9.86 % in the total intake of gas during the filling cycle, as seen in Table 4.

5.3 Cylindrical tanks with high heat capacity materials

The impact of the increase of the heat capacity of the non-adsorbent material is studied here by considering the cylindrical domain shown in Fig. 22. Materials presenting high heat capacity can be used to roughly approximate phase-change materials (PCM) (Toledo et al. 2013). This example is based on the parameters listed in Table 5, considering natural heat convection and a non-adsorbent material presenting specific heat capacity four times higher than Steel ($Cp_{non} = 1880$ J/kg.K). A different strategy of penalisation continuation is adopted here, starting at $p_{ini} = 20$ and increasing the penaliser by $\Delta_p = 10$ every 10 optimiser iterations.

Figure 23 shows the resulting topology for this case, where the non-adsorbent regions are not necessarily connected to the gas inlet or to the walls, given that materials with high heat capacity act as heat sinks. The distribution of the optimised filtered pseudo-porosity is shown in Fig. 24.

The convergence of the functional is shown in Fig. 25. It can be seen a different behaviour when compared to previous cases (Figs. 12 and 19), where the functional converges to lower values as the penalisation is increased. In previous cases, the low initial penalisation ($p = 1$) allows the occurrence of materials presenting intermediate properties, which would be a good solution if they were feasible. The main concept of the material model based on offset hyperbolic tangents is here verified, as it makes intermediate materials less interesting as the penalisation increases. Given that the optimisation of the cylindrical case starts from a moderate penalisation ($p = 20$), optimised layouts exploring artificial intermediate materials are not interesting from the beginning and the functional value increases along the iterations.

Non-adsorbent islands posses a radius of influence around them, resulting in an overall decrease of the adsorbent bed temperature, as seen in Fig. 26. Thereafter, the gas density field depicted in Fig. 27 becomes much more flat. Comparing with the homogeneous case, the mass of

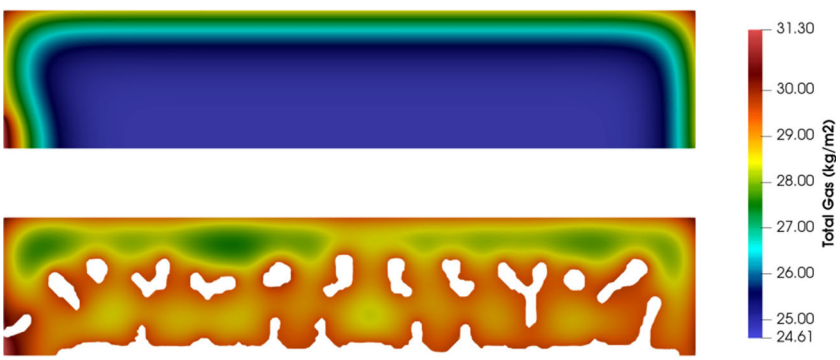


Fig. 27 Total gas distribution in homogeneous (top) and optimised cylindrical (bottom) tanks with high heat capacity material sections at the end of the adsorption cycle

Table 6 Total gas intake in homogeneous and optimised cylindrical tanks with high heat capacity material

	Gas intake (J_a)
Homogenous tank:	2.10 kg
Optimised tank:	2.31 kg
Improvement:	10.00%

gas admitted during the filling cycle is 10.00% higher when compared with the domain filled with activated carbon only, as shown in Table 6.

5.4 Remarks on the initial guess and penalisation

Topology optimisation problems are non-convex and often lead to different solutions depending on the initial guess and

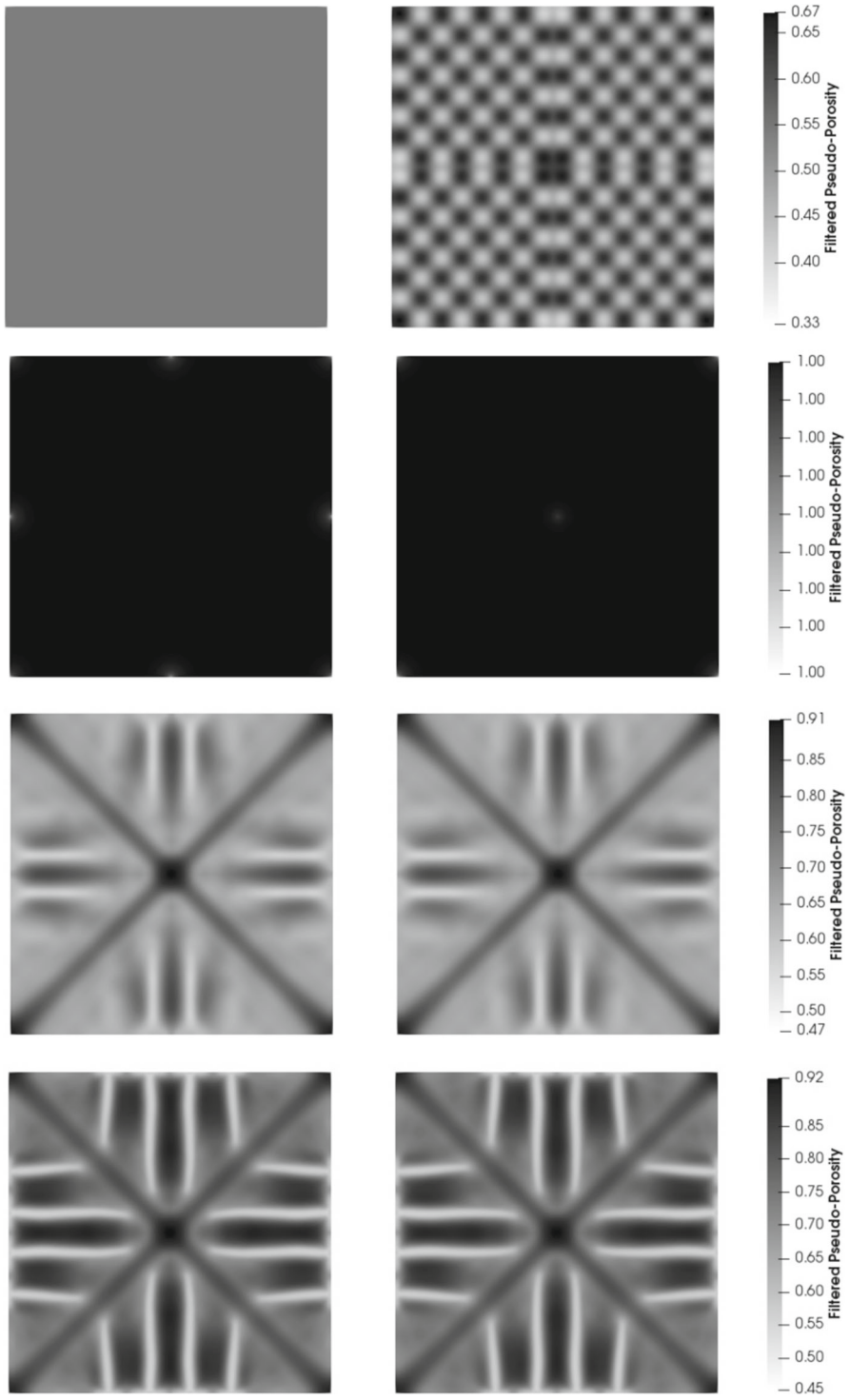


Fig. 28 Pseudo-porosity fields evolution for homogeneous (left) and arbitrary (right) initial guesses for prismatic tank optimisation starting with $p_{ini} = 1$

on the strategy adopted for the penalisation continuation on the material model.

The optimisation of the prismatic tank presented in Section 5.1 has been shown independent of the initial guess, as seen in Fig. 28, where the evolution of the optimisation starting from an homogeneous pseudo-porosity distribution $\mathbf{e} = \mathbf{0.5}$ is shown on the left column while one starting from an arbitrary initial guess is shown on the right. In both cases, the distribution of pseudo-porosities goes towards a full-carbon domain during the first optimisation iterations, following an identical evolution after that towards the same final layout.

The cylindrical tank optimisation presented in Section 5.3 is ran from a material model which is already significantly penalised ($p_{ini} = 20$). In this case, different initial guesses result in different final layouts as seen in Fig. 29, where the distributions on the top of each block show the evolution of the homogeneous initial guess, while the bottom ones refers to an arbitrary initial distribution of pseudo-porosity. Totally different layouts are obtained for each case, although the final objective function values are very similar: 2.31 kg of total gas intake for the homogeneous initial guess and 2.28 kg for the arbitrary.

The dependence of the final layouts on the initial guesses can be mitigated by following a continuation approach starting from a material model presenting low penalisation. Figure 30 shows the evolution of the pseudo-porosity distribution for an optimisation starting with penalisation $p_{ini} = 1$. Similar to the prismatic case, shown in Fig. 28, the initial optimisation steps take the pseudo-porosities to a full-carbon distribution, following the same evolution from then on. The final layout for this case results in a total gas intake of 2.30 kg, which is very similar to the 2.31 kg observed for the case starting the penalisation from $p_{ini} = 20$. This particular case also highlights the non-convexity of such optimisation problem, where a particular distribution of pseudo-porosities in a moderately penalised material model complies the objective function better than a less penalised one following a smooth continuation.

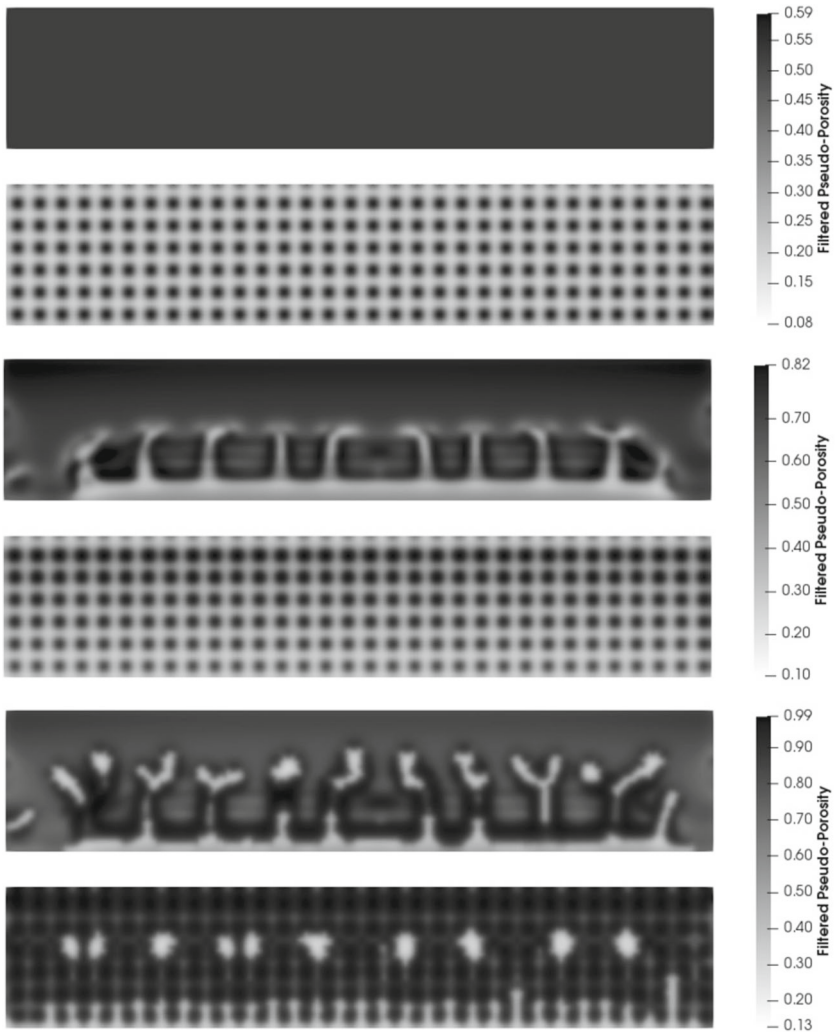


Fig. 29 Pseudo-porosity fields evolution for homogeneous (top image on each block) and arbitrary (bottom) initial guesses for cylindrical tank optimisation starting with $p_{ini} = 20$

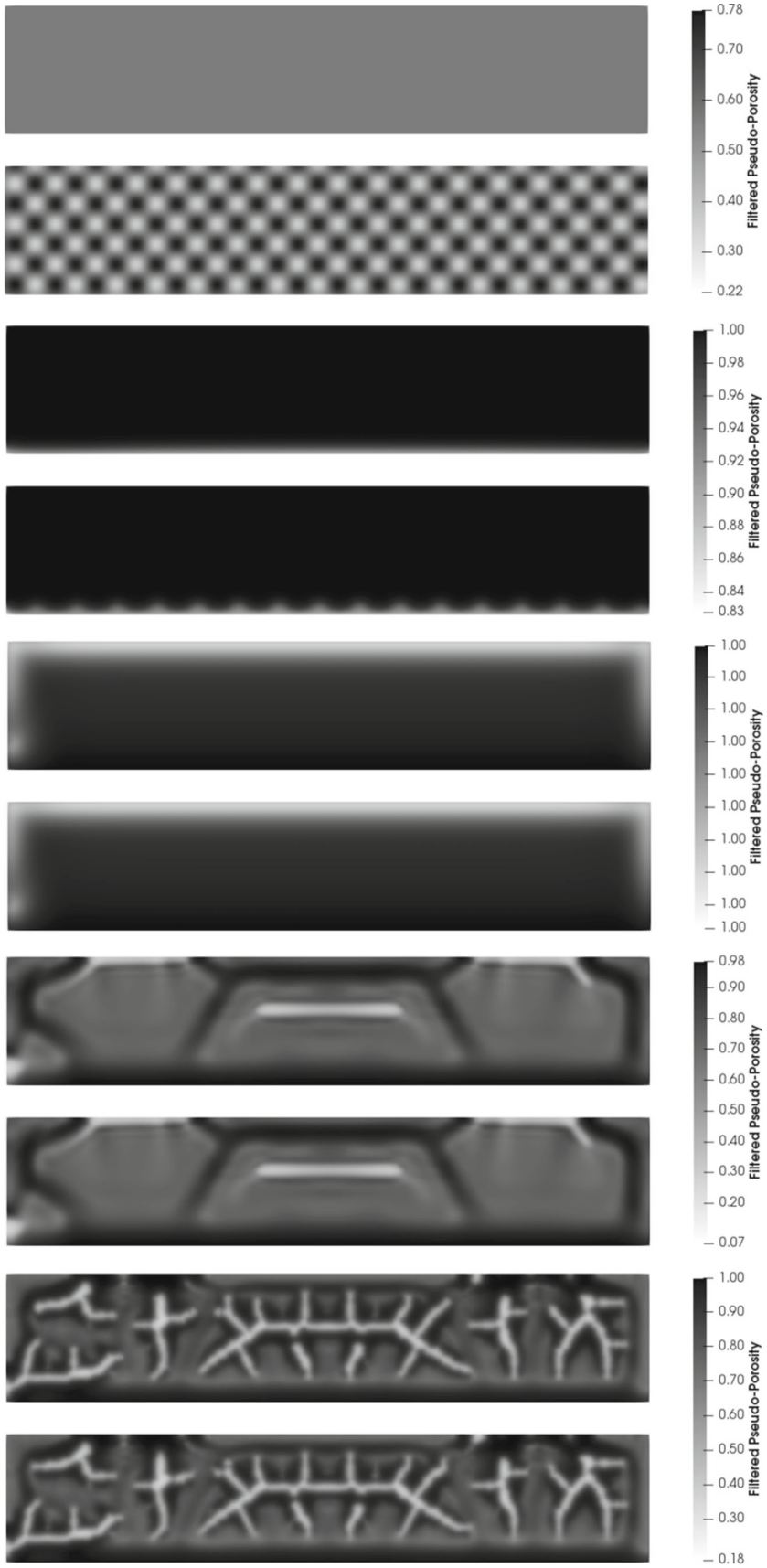


Fig. 30 Pseudo-porosity fields evolution for homogeneous (top image on each block) and arbitrary (bottom) initial guesses for cylindrical tank optimisation starting with $p_{ini} = 1$

6 Conclusions

In this work, a topology optimisation method for the design of adsorption systems is formulated and tested for ANG tanks. Accordingly, a comprehensive model for ANG tanks is presented, including the kinetics of adsorption and the variation of adsorbent properties in function to the porosities. The solution of the resulting set of PDEs governing the adsorption problem is obtained via FEM. The procedure to assemble the FEM matrices from the PDEs weak form is described in detail. The implementation of this method is based on the calculation of the sensitivities via the adjoint method for transient systems, which is comprehensively presented.

Examples of ANG tanks of different shapes subjected to different boundary conditions are studied. Tanks with optimised distribution of non-adsorbent materials presented significant gains in the total mass of gas admitted during the filling cycle in comparison to tanks constituted solely by an adsorbent material. The improvements in total gas mass intake observed are 6.03% in a prismatic tank subjected to forced convection, 9.86% in a complex axisymmetric tank subjected to natural convection and a cold wall, and 10.00% in a cylindrical tank subjected to natural convection with an optimised distribution of a high heat capacity phase.

Topology optimisation has been proven to be a suitable approach for optimising the distribution of different phases across adsorbent beds to improve gas storage. In particular, good results were achieved for biphasic adsorbent beds constituted by materials presenting high heat capacity, encouraging further research on the use of phase-change materials (PCM) in ANG tanks.

Funding information This paper received the support of the RCGI Research Centre for Gas Innovation, sponsored by FAPESP (2014/50279-4) and Shell. Authors also acknowledge the financial support of CNPq (National Council for Research and Development) under grants 140664/2013-0, 304121/2013-4 and 200404/2014-8.

Open Access This article is distributed under the terms of the Creative Commons Attribution 4.0 International License (http://creativecommons.org/licenses/by/4.0/), which permits unrestricted use, distribution, and reproduction in any medium, provided you give appropriate credit to the original author(s) and the source, provide a link to the Creative Commons license, and indicate if changes were made.

Appendix A: Finite element formulation

FEM is based on a weak formulation to approximate solutions for a set of PDEs by satisfying an integral problem for a family of test functions, v. Consider the domain $\Omega \subset \mathbb{R}^n$ and the Hilbert space $H^1(\Omega)$. The weak formulation of $\mathbb{L}(w)$ is given by its actuation on the test function v as (Karniadakis et al. 2005):

$$\langle \mathbb{L}(w), v\rangle = \int_\Omega \mathbb{L}(w)\, v\, d\mathbf{x} \forall v \in H^1(\Omega) \tag{46}$$

For axisymmetric domains, it is multiplied by $2\pi r$ and given by:

$$\langle \mathbb{L}(w), v\rangle = 2\pi \int_\Omega r\, \mathbb{L}(w)\, v\, d\mathbf{x} \forall v \in H^1(\Omega) \tag{47}$$

where r is the radial coordinate.

On $\Gamma_N \subset \partial\Omega$, where Robin boundary condition applies, the weak term for axisymmetric domains is given by Karniadakis et al. (2005):

$$\langle \mathbb{L}(w), v\rangle_{\Gamma_N} = 2\pi \oint_{\Gamma_N} r\, \mathbb{L}(w) \cdot \mathbf{n}\, v\, ds \forall v \in H^1(\Omega) \tag{48}$$

Considering the Dirichlet boundary condition given by:

$$w = w_D \text{ on } \Gamma_D \tag{49}$$

the unknown w belongs to the space $\mathcal{W}$ defined as:

$$\mathcal{W} = \{w \in H^1(\Omega) : w = w_D \text{ on } \Gamma_D\} \tag{50}$$

in which $w_D \in H^{1/2}(\Omega)$.

A.1 Adsorption problem

From (17), (23) and (13), the following weak forms are obtained for mass and energy balances and for the adsorption rate:

$$\begin{aligned}\mathbb{M} = &\left\langle \frac{\varepsilon_t M_g}{R_g}\frac{1}{T}\frac{\partial P}{\partial t}, v_M\right\rangle - \left\langle \frac{\varepsilon_t M_g}{R_g}\frac{P}{T^2}\frac{\partial T}{\partial t}, v_M\right\rangle \\ &+\left\langle \frac{\partial Q}{\partial t}, v_M\right\rangle + \left\langle \frac{M_g K_s}{R_g \mu_g}\frac{P}{T}\nabla P, \nabla v_M\right\rangle \\ &-\left\langle \frac{M_g K_s}{R_g \mu_g}\frac{P}{T}\nabla P, v_M\right\rangle_{\Gamma_N} = 0, \\ &\forall v_M \in H^1(\Omega)\end{aligned} \tag{51}$$

$$\begin{aligned}\mathbb{E} = &\left\langle \frac{\varepsilon_t C p_g M_g}{R_g}\frac{P}{T}\frac{\partial T}{\partial t}, v_E\right\rangle + \left\langle C p_g Q \frac{\partial T}{\partial t}, v_E\right\rangle \\ &+\left\langle (1-\varepsilon_t)\rho_s C p_s \frac{\partial T}{\partial t}, v_E\right\rangle - \left\langle \varepsilon_t \frac{\partial P}{\partial t}, v_E\right\rangle \\ &+\left\langle \frac{C p_g M_g K_s}{R_g \mu_g}\frac{P}{T}\nabla P \cdot \nabla T, \nabla v_E\right\rangle \\ &+\langle k_f \nabla T, \nabla v_E\rangle - \left\langle |\Delta H| \frac{\partial Q}{\partial t}, v_E\right\rangle \\ &-\left\langle \frac{C p_g M_g K_s}{R_g \mu_g}\frac{P}{T}\nabla P \cdot \nabla T, v_E\right\rangle_{\Gamma_N} \\ &-\langle k_f \nabla T, v_E\rangle_{\Gamma_N} = 0, \\ &\forall v_E \in H^1(\Omega)\end{aligned} \tag{52}$$

$$\mathbb{D} = \left\langle \frac{\partial Q}{\partial t}, v_D \right\rangle + \langle GQ, v_D \rangle - \langle GQ_{eq}, v_D \rangle = 0, \quad \forall v_D \in H^1(\Omega) \tag{53}$$

Given the convective heat transfer on the walls:

$$\langle k_f \nabla T, v_E \rangle_{\Gamma_N} = -\langle h_W (T - T_\infty), v_E \rangle_{\Gamma_W} \tag{54}$$

The weak forms of the adsorption problem are approximated over a finite element, ω, by the following expressions (Hess et al. 2016):

$$P(\mathbf{x}, t) \cong \sum_{n=1}^{N} \phi_n(\mathbf{x}) P_n(t) = \mathbf{\Phi}^T \mathbf{P} \tag{55}$$

$$T(\mathbf{x}, t) \cong \sum_{m=1}^{M} \psi_m(\mathbf{x}) T_m(t) = \mathbf{\Psi}^T \mathbf{T} \tag{56}$$

where $\mathbf{P}$ and $\mathbf{T}$ are, respectively, the vectors with the nodal values of pressure and temperature, N and M denotes the number of nodes used for each unknown and ϕ and ψ are the shape functions, which are assembled in matrices $\mathbf{\Phi}$ and $\mathbf{\Psi}$.

Analogously, the mass of adsorbed gas per volume of adsorbent (Q) is interpolated over finite elements by the shape function ξ:

$$Q(\mathbf{x}, t) \cong \sum_{l=1}^{L} \xi_l(\mathbf{x}) Q_l(t) = \mathbf{\Xi}^T \mathbf{Q} \tag{57}$$

The interpolation of the total porosity (ε) and all other material properties is also done by using ξ:

$$\varepsilon(\mathbf{x}, t) \cong \sum_{l=1}^{L} \xi_l(\mathbf{x}) \varepsilon_l(t) = \mathbf{\Xi}^T \boldsymbol{\varepsilon} \tag{58}$$

Making $v_M = \phi$, $v_E = \psi$ and $v_D = \xi$, the FEM system is assembled based on the following coefficients:

$$M_{tp}(T) = \int_\omega [2\pi r] \frac{M_g(\mathbf{\Xi}^T \boldsymbol{\varepsilon}_t)}{R_g(\mathbf{\Psi}^T \mathbf{T})} \mathbf{\Phi}\mathbf{\Phi}^T d\mathbf{x} \tag{59}$$

$$M_{tt}(P, T) = \int_\omega [2\pi r] \frac{M_g(\mathbf{\Xi}^T \boldsymbol{\varepsilon}_t)(\mathbf{\Phi}^T \mathbf{P})}{R_g(\mathbf{\Psi}^T \mathbf{T})^2} \mathbf{\Phi}\mathbf{\Psi}^T d\mathbf{x} \tag{60}$$

$$M_{tq} = \int_\omega [2\pi r] \, \mathbf{\Phi}\mathbf{\Xi}^T dx \tag{61}$$

$$E_{tp} = \int_\omega [2\pi r] \, (\mathbf{\Xi}^T \boldsymbol{\varepsilon}_t) \mathbf{\Psi}\mathbf{\Phi}^T d\mathbf{x} \tag{62}$$

$$E_{tt}(P, T, Q) = \int_\omega [2\pi r] \frac{Cp_g M_g(\mathbf{\Xi}^T \boldsymbol{\varepsilon_t})}{R_g} \frac{(\mathbf{\Phi}^T \mathbf{P})}{(\mathbf{\Psi}^T \mathbf{T})} \mathbf{\Psi}\mathbf{\Psi}^T d\mathbf{x} + \int_\omega [2\pi r] \, Cp_g(\mathbf{\Xi}^T \mathbf{Q}) \mathbf{\Psi}\mathbf{\Psi}^T d\mathbf{x} + \int_\omega [2\pi r] \, (1 - \mathbf{\Xi}^T \boldsymbol{\varepsilon}_t)(\mathbf{\Xi}^T \mathbf{Cp_s})(\mathbf{\Xi}^T \boldsymbol{\rho}_s) \mathbf{\Psi}\mathbf{\Psi}^T d\mathbf{x} \tag{63}$$

$$E_{tq} = \int_\omega -[2\pi r] \, |\Delta H| \mathbf{\Psi}\mathbf{\Xi}^T dx \tag{64}$$

$$D_{tq} = \int_\omega [2\pi r] \, \mathbf{\Xi}\mathbf{\Xi}^T dx \tag{65}$$

$$M_{sp}(P, T) = \int_\omega [2\pi r] \frac{M_g(\mathbf{\Xi}^T \mathbf{K_s})(\mathbf{\Phi}^T \mathbf{P})}{R_g \mu_g(\mathbf{\Psi}^T \mathbf{T})} \nabla\mathbf{\Phi}\nabla\mathbf{\Phi}^T d\mathbf{x} - \int_{\gamma_W} [2\pi r] \frac{M_g(\mathbf{\Xi}^T \mathbf{K_s})(\mathbf{\Phi}^T \mathbf{P})}{R_g \mu_g(\mathbf{\Psi}^T \mathbf{T})} \mathbf{\Phi}\nabla\mathbf{\Phi}^T ds \tag{66}$$

$$E_{st}(P, T) = \int_\omega [2\pi r] \, (\mathbf{\Xi}^T \mathbf{k_f}) \nabla\mathbf{\Psi}\nabla\mathbf{\Psi}^T d\mathbf{x} - \int_\omega [2\pi r] \frac{Cp_g M_g(\mathbf{\Xi}^T \mathbf{K_s})(\mathbf{\Phi}^T \mathbf{P})}{R_g \mu_g(\mathbf{\Psi}^T \mathbf{T})} \times (\nabla\mathbf{\Phi}^T \mathbf{P}) \nabla\mathbf{\Psi}\nabla\mathbf{\Psi}^T d\mathbf{x} - \int_{\gamma_W} [2\pi r] \, (\mathbf{\Xi}^T \mathbf{k_f}) \mathbf{\Psi}\nabla\mathbf{\Psi}^T ds \tag{67}$$

$$D_{sq}(T) = \int_\omega [2\pi r] \, (\mathbf{\Xi}^T \mathbf{G}) \mathbf{\Xi}\mathbf{\Xi}^T d\mathbf{x} \tag{68}$$

$$D_r(P, T) = \int_\omega [2\pi r] \, (\mathbf{\Xi}^T \mathbf{G})(\mathbf{\Xi}^T \mathbf{Q_{eq}}) \mathbf{\Xi} d\mathbf{x} \tag{69}$$

A.2 Helmholtz filtering

The weak form of the modified Helmholtz-type PDE is given by:

$$\mathbb{H} = \langle \mathrm{e}, v_H \rangle + \left\langle z^2 \nabla \mathrm{e}, \nabla v_H \right\rangle = \langle \mathrm{\phi}, v_H \rangle, \quad \forall v_H \in H^1(\Omega) \tag{70}$$

The interpolation of the pseudo-porosities is done over a finite element by using the shape function ξ:

$$\mathrm{e}(\mathbf{x}, t) \cong \sum_{l=1}^{L} \xi_l(\mathbf{x}) \mathrm{e}(t) = \mathbf{\Xi}^T \mathbf{e} \tag{71}$$

Making $v_H = \xi$, the FEM system is assembled based on the following coefficients:

$$Z = \int_\omega \mathbf{\Xi}\mathbf{\Xi}^T d\mathbf{x} + \int_\omega z^2 \nabla\mathbf{\Xi}\nabla\mathbf{\Xi}^T d\mathbf{x} \tag{72}$$

$$\mathrm{\phi} = \int_\omega (\mathbf{\Xi}^T \, \mathrm{\phi}) \mathbf{\Xi} d\mathbf{x} \tag{73}$$

A.3 Derivation of the adjoint problem

In the optimisation problem given in (30), the functional of interest $J_a(\mathbf{w}(\mathbf{e}), \mathbf{e})$ is constrained to the PDE system $\mathbf{F}(\mathbf{w}, \mathbf{e}) = \mathbf{0}$ given in (33). The difference in the total gas mass between the beginning and the end of the adsorption cycle can be expressed in terms of Dirac's delta

inside a time-integral, resulting in the following augmented Lagrangian form:

$$J_a = \int_{t_{ia}}^{t_{fa}} \left(\delta_{t_{fa}} - \delta_{t_{ia}}\right) B + \boldsymbol{\lambda}^T \left(\mathbf{F}_t \dot{\mathbf{w}} + \mathbf{F}_s \mathbf{w} - \mathbf{F}_r\right) dt \quad (74)$$

where B denotes the total gas mass, given by:

$$B = \int_{\Omega} (Q + \rho_g) dx \quad (75)$$

and, for simplicity:

$$\delta_{t_{fa}} - \delta_{t_{ia}} = \delta(t - t_{fa}) - \delta(t - t_{ia}) \quad (76)$$

where δ denotes Dirac's delta operator.

The vector of Lagrange multipliers, $\boldsymbol{\lambda}$, is given by:

$$\boldsymbol{\lambda} = \left\{ \begin{array}{c} \boldsymbol{\lambda}_M \\ \boldsymbol{\lambda}_E \\ \boldsymbol{\lambda}_D \end{array} \right\} \quad (77)$$

The derivative of the reduced functional J in respect to a design variable e_j is given by:

$$\begin{aligned} \frac{dJ_a}{d\mathrm{e}_j} = & \int_{t_{ia}}^{t_{fa}} \left(\delta_{t_{fa}} - \delta_{t_{ia}}\right) \left(\frac{\partial B}{\partial \mathrm{e}_j} + \frac{\partial B}{\partial \mathbf{w}} \frac{d\mathbf{w}}{d\mathrm{e}_j}\right) dt \\ & + \int_{t_{ia}}^{t_{fa}} \boldsymbol{\lambda}^T \left[\left(\frac{\partial \mathbf{F}_t}{\partial \mathrm{e}_j} + \frac{\partial \mathbf{F}_t}{\partial \mathbf{w}} \frac{d\mathbf{w}}{d\mathrm{e}_j} \right) \dot{\mathbf{w}} + \mathbf{F}_t \frac{d\dot{\mathbf{w}}}{d\mathrm{e}_j} \right. \\ & + \left(\frac{\partial \mathbf{F}_s}{\partial \mathrm{e}_j} + \frac{\partial \mathbf{F}_s}{\partial \mathbf{w}} \frac{d\mathbf{w}}{d\mathrm{e}_j} \right) \mathbf{w} \\ & \left. + \mathbf{F}_s \frac{d\mathbf{w}}{d\mathrm{e}_j} - \frac{\partial \mathbf{F}_r}{\partial \mathrm{e}_j} - \frac{\partial \mathbf{F}_r}{\partial \mathbf{w}} \frac{d\mathbf{w}}{d\mathrm{e}_j} \right] dt \end{aligned} \quad (78)$$

Integrating the term involving $d\dot{\mathbf{w}}/d\mathrm{e}_j$ by parts, results in:

$$\frac{dJ_a}{d\mathrm{e}_j} = \Theta_{sen} + \Theta_{b,ia} + \Theta_{b,fa} + \Theta_{adj} \quad (79)$$

where:

$$\begin{aligned} \Theta_{sen} = & \int_{t_{ia}}^{t_{fa}} \left[\left(\delta_{t_{fa}} - \delta_{t_{ia}}\right) \frac{\partial B}{\partial \mathrm{e}_j} \right. \\ & \left. + \boldsymbol{\lambda}^T \left(\frac{\partial \mathbf{F}_t}{\partial \mathrm{e}_j} \dot{\mathbf{w}} + \frac{\partial \mathbf{F}_s}{\partial \mathrm{e}_j} \mathbf{w} - \frac{\partial \mathbf{F}_r}{\partial \mathrm{e}_j} \right) \right] dt \end{aligned} \quad (80)$$

$$\Theta_{b,ia} = - \boldsymbol{\lambda}^T \mathbf{F}_t \frac{d\mathbf{w}}{d\mathrm{e}_j}\bigg|_{t_{ia}} \quad (81)$$

$$\Theta_{b,fa} = \boldsymbol{\lambda}^T \mathbf{F}_t \frac{d\mathbf{w}}{d\mathrm{e}_j}\bigg|_{t_{fa}} \quad (82)$$

$$\begin{aligned} \Theta_{adj} = & \int_{t_{ia}}^{t_{fa}} \frac{d\mathbf{w}}{d\mathrm{e}_j} \left[\left(\delta_{t_{fa}} - \delta_{t_{ia}}\right) \frac{\partial B}{\partial \mathbf{w}} - \frac{\partial (\boldsymbol{\lambda}^T \mathbf{F}_t)}{\partial t} \right. \\ & \left. + \boldsymbol{\lambda}^T \left(\mathbf{F}_s + \frac{\partial \mathbf{F}_t}{\partial \mathbf{w}} \dot{\mathbf{w}} + \frac{\partial \mathbf{F}_s}{\partial \mathbf{w}} \mathbf{w} - \frac{\partial \mathbf{F}_r}{\partial \mathbf{w}} \right) \right] dt \end{aligned} \quad (83)$$

Regarding the derivatives of $\mathbf{w}$ at the initial time t_{ia}, although P_{ia} and T_{ia} are imposed and do not depend on the design variables, the initial density of gas adsorbed, Q_{ia}, is dependent on the volume of adsorbent material inside the domain. Therefore, the derivative of the state variables in respect to e_j is given by:

$$\left.\frac{d\mathbf{w}}{d\mathrm{e}_j}\right|_{t_{ia}} = \left\{ \begin{array}{c} 0 \\ 0 \\ Q_{eq}(P_{ia}, T_{ia}) \frac{dm(\mathrm{e}_j)}{d\mathrm{e}_j} \end{array} \right\} \quad (84)$$

where the equilibrium adsorbed density Q_{eq} is given in (9) and the material model interpolation function $m(\mathrm{e}_j)$ is given in (28).

Since the term $d\mathbf{w}/d\mathrm{e}_j$ is unknown for $t > t_{ia}$, the terms $\Theta_{b,fa}$ and Θ_{adj} cannot be evaluated explicitly. Given that $\boldsymbol{\lambda}$ is arbitrary, it can be chosen in order to nullify these terms (Dahl et al. 2008). To ensure $\Theta_{b,fa} = 0$ it is necessary to choose $\boldsymbol{\lambda}$ such that $\boldsymbol{\lambda}(t_{fa}) = \mathbf{0}$. The term Θ_{adj} is null when the expression between brackets is equal to zero, which can be rewritten as:

$$\begin{aligned} & \left(\delta_{t_{fin}} - \delta_{t_{ini}}\right) \frac{\partial B}{\partial \mathbf{w}} - \dot{\boldsymbol{\lambda}}^T \mathbf{F}_t - \boldsymbol{\lambda}^T \frac{\partial \mathbf{F}_t}{\partial \mathbf{w}} \frac{d\mathbf{w}}{dt} \\ & + \boldsymbol{\lambda}^T \left(\mathbf{F}_s + \frac{\partial \mathbf{F}_t}{\partial \mathbf{w}} \frac{d\mathbf{w}}{dt} + \frac{\partial \mathbf{F}_s}{\partial \mathbf{w}} \mathbf{w} - \frac{\partial \mathbf{F}_r}{\partial \mathbf{w}} \right) = 0 \end{aligned} \quad (85)$$

resulting in:

$$\begin{aligned} & \left(\delta_{t_{fa}} - \delta_{t_{ia}}\right) \frac{\partial B}{\partial \mathbf{w}} - \dot{\boldsymbol{\lambda}}^T \mathbf{F}_t \\ & + \boldsymbol{\lambda}^T \left(\mathbf{F}_s + \frac{\partial \mathbf{F}_s}{\partial \mathbf{w}} \mathbf{w} - \frac{\partial \mathbf{F}_r}{\partial \mathbf{w}} \right) = 0 \end{aligned} \quad (86)$$

The Lagrange multiplier $\boldsymbol{\lambda}$ is then given by the solution of the following adjoint problem:

$$\begin{aligned} \left(\mathbf{F}_t(\mathbf{w})\right)^T \dot{\boldsymbol{\lambda}}(t) - \left(\mathbf{F}_u(\mathbf{w})\right)^T \boldsymbol{\lambda}(t) &= \left(\delta_{t_{fa}} - \delta_{t_{ia}}\right) \frac{\partial B}{\partial \mathbf{w}} \\ \boldsymbol{\lambda}(t_{fa}) &= \mathbf{0} \end{aligned} \quad (87)$$

where, for simplicity:

$$\mathbf{F}_u(\mathbf{w}) = \mathbf{F}_s(\mathbf{w}) + \frac{\partial \mathbf{F}_s(\mathbf{w})}{\partial \mathbf{w}} \mathbf{w} - \frac{\partial \mathbf{F}_r(\mathbf{w})}{\partial \mathbf{w}} \quad (88)$$

Such system poses a terminal value problem, which can be converted to an initial value problem by substituting the time variable t per $\tau = t_{fa} - t$. A new system is then defined in terms of $\bar{\boldsymbol{\lambda}}(\tau) = \boldsymbol{\lambda}(t_{fa} - t)$:

$$\begin{aligned} \left(\mathbf{F}_t(\mathbf{w})\right)^T \dot{\bar{\boldsymbol{\lambda}}}(\tau) + \left(\mathbf{F}_u(\mathbf{w})\right)^T \bar{\boldsymbol{\lambda}}(\tau) &= \left(\delta_{\tau_{fa}} - \delta_{\tau_{ia}}\right) \frac{\partial B}{\partial \mathbf{w}} \\ \bar{\boldsymbol{\lambda}}(\tau_{ia}) &= \mathbf{0} \end{aligned} \quad (89)$$

Letting the Laplace transform of $\bar{\boldsymbol{\lambda}}(\tau)$ be expressed as:

$$\mathcal{L}\{\bar{\boldsymbol{\lambda}}(\tau)\} = \bar{\boldsymbol{\Lambda}}(s) \tag{90}$$

The transformation of first two terms in the (89) gives:

$$\mathcal{L}\left\{(\mathbf{F}_t(\mathbf{w}))^T\,\dot{\bar{\boldsymbol{\lambda}}}(\tau)\right\} = (\mathbf{F}_t(\mathbf{w}))^T\left(s\bar{\boldsymbol{\Lambda}}(s) - \bar{\boldsymbol{\lambda}}(\tau_{ia})\right) \tag{91}$$

$$\mathcal{L}\left\{(\mathbf{F}_u(\mathbf{w}))^T\,\bar{\boldsymbol{\lambda}}(\tau)\right\} = (\mathbf{F}_u(\mathbf{w}))^T\,\bar{\boldsymbol{\Lambda}}(s) \tag{92}$$

From the definition of the Laplace transform, the transformation of the last term is given by:

$$\mathcal{L}\left\{\left(\delta_{\tau_{fa}} - \delta_{\tau_{ia}}\right)\frac{\partial B}{\partial \mathbf{w}}\right\} = \int_0^\infty e^{-s\tau}\left(\delta_{\tau_{fa}} - \delta_{\tau_{ia}}\right)\frac{\partial B}{\partial \mathbf{w}}d\tau \tag{93}$$

which results in:

$$\mathcal{L}\left\{\left(\delta_{\tau_{fa}} - \delta_{\tau_{ia}}\right)\frac{\partial B}{\partial \mathbf{w}}\right\} = \left(e^{-s\tau_{fa}} - e^{-s\tau_{ia}}\right)\mathcal{L}\left\{\frac{\partial B}{\partial \mathbf{w}}\right\} \tag{94}$$

Following, the inverse Laplace transform must be performed to go back to the reverse time domain τ, which for the last term is given by:

$$\begin{aligned}&\mathcal{L}^{-1}\left\{\left(e^{-s\tau_{fa}} - e^{-s\tau_{ia}}\right)\mathcal{L}\left\{\frac{\partial B(\tau)}{\partial \mathbf{w}}\right\}\right\}\\ &= H(\tau - \tau_{fa})\frac{\partial B(\tau - \tau_{fa})}{\partial \mathbf{w}} - H(\tau - \tau_{ia})\frac{\partial B(\tau - \tau_{ia})}{\partial \mathbf{w}}\end{aligned} \tag{95}$$

where H denotes the heaviside step function, which is applied to the function B shifted by τ_{fa} and τ_{ia}.

The adjoint problem given in (89) becomes:

$$\begin{aligned}&(\mathbf{F}_t(\mathbf{w}))^T\,\dot{\bar{\boldsymbol{\lambda}}}(\tau) + (\mathbf{F}_u(\mathbf{w}))^T\,\bar{\boldsymbol{\lambda}}(\tau)\\ &\quad = H_{\tau_{fa}}\frac{\partial B_{\tau_{fa}}}{\partial \mathbf{w}} - H_{\tau_{ia}}\frac{\partial B_{\tau_{ia}}}{\partial \mathbf{w}}\\ &\qquad\qquad \bar{\boldsymbol{\lambda}}(\tau_{ia}) = \mathbf{0}\end{aligned} \tag{96}$$

where, for simplicity:

$$\begin{aligned}&H_{\tau_{fa}}\frac{\partial B_{\tau_{fa}}}{\partial \mathbf{w}} - H_{\tau_{ia}}\frac{\partial B_{\tau_{ia}}}{\partial \mathbf{w}}\\ &= H(\tau - \tau_{fa})\frac{\partial B(\tau - \tau_{fa})}{\partial \mathbf{w}} - H(\tau - \tau_{ia})\frac{\partial B(\tau - \tau_{ia})}{\partial \mathbf{w}}\end{aligned} \tag{97}$$

The discretisation of the adjoint system in time via implicit Euler method results in:

$$\mathbf{A}\begin{Bmatrix}\bar{\boldsymbol{\lambda}}_0\\ \bar{\boldsymbol{\lambda}}_1\\ \vdots\\ \bar{\boldsymbol{\lambda}}_{N-1}\\ \bar{\boldsymbol{\lambda}}_N\end{Bmatrix} = \begin{Bmatrix}\mathbf{0}\\ \mathbf{A}_R(\mathbf{w}_1)\\ \vdots\\ \mathbf{A}_R(\mathbf{w}_{N-1})\\ \mathbf{A}_R(\mathbf{w}_N)\end{Bmatrix} \tag{98}$$

where the matrix $\mathbf{A}$ is given by:

$$\mathbf{A} = \begin{bmatrix}\mathbf{I} & \mathbf{0} & \cdots & \mathbf{0} & \mathbf{0}\\ \mathbf{A}_P(\mathbf{w}_0) & \mathbf{A}_C(\mathbf{w}_1) & \cdots & \mathbf{0} & \mathbf{0}\\ \vdots & \vdots & \ddots & \vdots & \vdots\\ \mathbf{0} & \mathbf{0} & \cdots & \mathbf{A}_P(\mathbf{w}_{N-1}) & \mathbf{A}_C(\mathbf{w}_N)\end{bmatrix} \tag{99}$$

in which:

$$\mathbf{A}_P(\mathbf{w}_n) = \left(-\frac{\mathbf{F}_t(\mathbf{w}_n)}{\Delta t}\right)^T \tag{100}$$

$$\begin{aligned}\mathbf{A}_C(\mathbf{w}_n) = \Bigg(&\frac{\mathbf{F}_t(\mathbf{w}_n)}{\Delta t} + \mathbf{F}_s(\mathbf{w}_n)\\ &+ \frac{\partial \mathbf{F}_s(\mathbf{w}_n)}{\partial \mathbf{w}_n}\mathbf{w}_n - \frac{\partial \mathbf{F}_r(\mathbf{w}_n)}{\partial \mathbf{w}_n}\Bigg)^T\end{aligned} \tag{101}$$

$$\mathbf{A}_R(\mathbf{w}_n) = H_{\tau_{fa}}\frac{\partial B_{\tau_{fa}}}{\partial \mathbf{w}_n} - H_{\tau_{ia}}\frac{\partial B_{\tau_{ia}}}{\partial \mathbf{w}_n} \tag{102}$$

The solution of the system above, in terms of $\bar{\boldsymbol{\lambda}}(\tau)$, is then reversed in time to obtain $\boldsymbol{\lambda}(t)$.

Appendix B: Sensitivities verification

The topology optimisation relies on the accurate computation of the sensitivity of the objective functions to the design variables. The gradients computed based on the adjoint problem described in Appendix A.3 can be verified through a Taylor remainder convergence test. Given a reduced functional $\hat{J}(m)$ subjected to an arbitrary perturbation δm, the first-order Taylor remainder tends to zero at $\mathcal{O}(h)$ while the second-order tends at $\mathcal{O}(h^2)$. That means that by halving h the first-order error also halves while the second-order error is divided by four. Taylor remainders expressions are given in (103). By evaluating the second-order remainder based on the $\nabla\hat{J}$ obtained via adjoint approach, its correctness can be determined by observing $\mathcal{O}(h^2)$ convergence.

$$\begin{aligned}&|\hat{J}(m + h\delta m) - \hat{J}(m)| \to 0 \;\; at\; \mathcal{O}(h)\\ &|\hat{J}(m + h\delta m) - \hat{J}(m) - h\nabla\hat{J}\cdot\delta m| \to 0 \;\; at\; \mathcal{O}(h^2)\end{aligned} \tag{103}$$

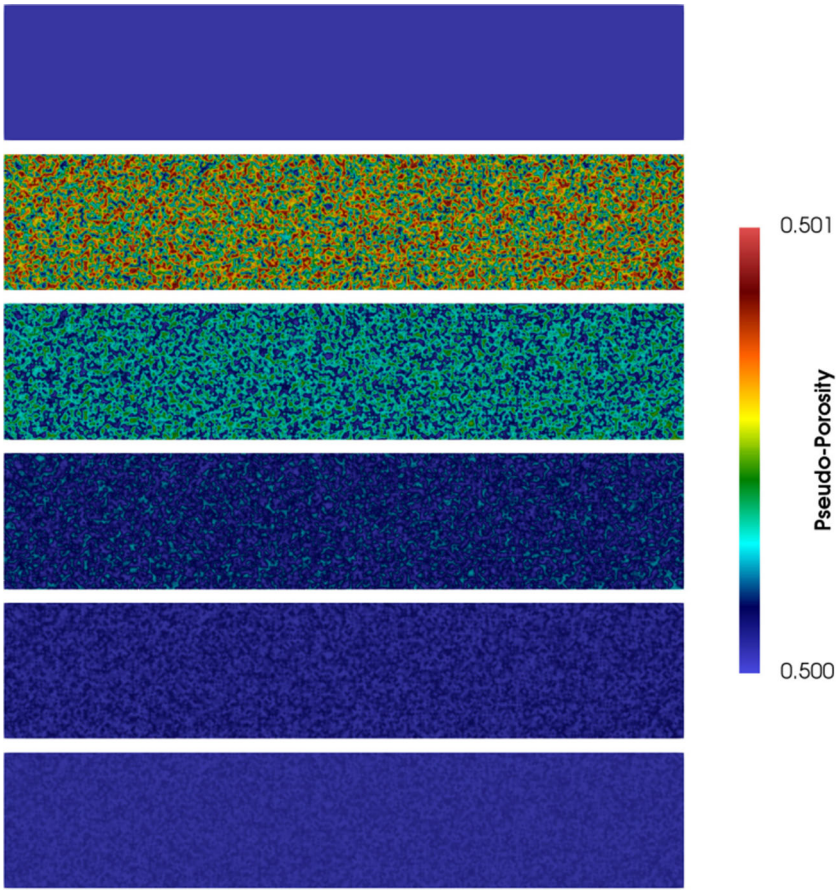


Fig. 31 Original (top) and Perturbed Pseudo-Porosity fields for (from the top) $h = 1.0 \times 10^{-3}$, $h = 5.0 \times 10^{-4}$, $h = 2.5 \times 10^{-5}$, $h = 1.25 \times 10^{-5}$, $h = 6.25 \times -6$

Figure 31 depicts the pseudo-random perturbation δe scaled to different values of h.

The remainders listed in Table 7 demonstrates the correctness of $\nabla \hat{J}$ as the convergence order of second-order Taylor remainders are approximately 2.0.

Table 7 First and second-order Taylor remainder convergence

h	Taylor remainder	Convergence order
1st order		
1.0×10^{-3}	1.471536×10^{-3}	
5.0×10^{-4}	7.361257×10^{-4}	0.99929
2.5×10^{-5}	3.681522×10^{-4}	0.99964
1.25×10^{-5}	1.840984×10^{-4}	0.99982
6.25×10^{-6}	9.205482×10^{-5}	0.99991
2nd order		
1.0×10^{-3}	1.430238×10^{-6}	
5.0×10^{-4}	3.575846×10^{-7}	1.99989
2.5×10^{-5}	8.939859×10^{-8}	1.99996
1.25×10^{-5}	2.234841×10^{-8}	2.00007
6.25×10^{-6}	5.586599×10^{-9}	2.00013

Appendix C: Material properties

Material properties adopted in the examples presented in Section 5 are listed here. The properties of methane and activated carbon are given in Tables 8 and 9, respectively. Parameters related to the adsorption of methane on activated

Table 8 Methane properties (Sahoo et al. 2011)

Property	Symbol	Value	Unit
Specific heat	Cp_g	14890	J/kg.K
Thermal conduct.	k_g	34.3×10^{-3}	W/m.K
Molar mass	M_g	16.03×10^{-3}	kg/mol
Critical pressure	P_{cr}	4.596×10^{6}	Pa
Boiling point temp.	T_{boil}	111.2	K
Critical temperature	T_{cr}	191	K
Th. Exp. Liq. gases	α_e	2.5×10^{-3}	1/K
Boiling point density	ρ_{boil}	422.62	kg/m^3
Viscosity	μ_g	12.5×10^{-6}	Pa.s

Table 9 Activated carbon properties (Sahoo et al. 2011)

Property	Symbol	Value	Unit
Bulk specific heat	Cp_s	650	J/kg.K
Bulk thermal conduct.	k_s	0.54	W/m.K
Micropores dispersion	n_s	1.8	
Spec. micropores vol.	w_s	0.33×10^{-3}	m^3/kg
Particle diameter	ϕ_s	1×10^{-3}	m
Macroporosity	ε_M	0.3	
Microporosity	ε_m	0.5	
Bulk density	ρ_s	1428.57	kg/m^3
Micropore tortuosity	τ_s	2.08	

Table 10 Adsorption parameters for methane on activated carbon (Sahoo et al. 2011)

Property	Symbol	Value	Unit
Eff. gas diffusivity	D_0	8.0×10^{-7}	m^2/s
Characteristic energy	E_0	25040	J/mol
Act. energy of adsorp.	E_a	6000	J/mol
Affinity coefficient	β	0.35	
Isost. heat of adsorp.	ΔH	-16000×10^3	J/mol

Table 11 Steel properties

Property	Symbol	Value	Unit
Specific heat	Cp_s	470	J/kg.K
Thermal conductivity	k_s	47	W/m.K
Density	ρ_s	7900	kg/m^3
Permeability	K_s	1.0×10^{-22}	m^2

carbon are given in Table 10. Optimised topologies are based on the distribution of steel across the adsorbent bed, which properties are given in Table 11.

Publisher's Note Springer Nature remains neutral with regard to jurisdictional claims in published maps and institutional affiliations.

References

Anagnostou G, Roenquist EM, Patera AT (1992) A computational procedure for part design. Comput Methods Appl Mech Eng 97(1):33 – 48. https://doi.org/10.1016/0045-7825(92)90106-T

Bendsøe MP, Sigmund O (1999) Material interpolation schemes in topology optimization. Arch Appl Mech 69(9-10):635–654. https://doi.org/10.1007/s004190050248

Biloė S, Goetz V, Guillot A (2002) Optimal design of an activated carbon for an adsorbed natural gas storage system. Carbon 40(8):1295–1308. https://doi.org/10.1016/S0008-6223(01)00287-1

Bird RB, Stewart WB, Lightfoot EN (2007) Transport Phenomena. 2nd edn

Blanco M, Borzone E, Baruj A, Meyer G (2014) Hydrogen sorption kinetics of la-ni-sn storage alloys. Int J Hydrog Energy 39(11):5858–5867. https://doi.org/10.1016/j.ijhydene.2014.01.125

Borrvall T, Petersson J (2003) Topology optimization of fluids in stokes flow. Int J Numer Methods Fluids 41(1):77–107. https://doi.org/10.1002/fld.426

Bruns TE (2007) Topology optimization of convection-dominated, steady-state heat transfer problems. Int J Heat Mass Transfer 50(15–16):2859–2873. https://doi.org/10.1016/j.ijheatmasstransfer.2007.01.039

Byrd R, Lu P, Nocedal J, Zhu C (1995) A limited memory algorithm for bound constrained optimization. SIAM J Sci Comput 16(5):1190–1208. https://doi.org/10.1137/0916069

Carman P (1937) Fluid flow through granular beds. Chem Eng Res Des 75:S32–S48. https://doi.org/10.1016/S0263-8762(97)80003-2

Chang KJ, Talu O (1996) Behavior and performance of adsorptive natural gas storage cylinders during discharge. Appl Therm Eng 16(5 SPEC. ISS.):359–374. https://doi.org/10.1016/1359-4311(95)00017-8

Dahl J, Jensen JS, Sigmund O (2008) Topology optimization for transient wave propagation problems in one dimension: Ddesign of filters and pulse modulators. Struct Multidiscip Optim 36(6):585–595. https://doi.org/10.1007/s00158-007-0192-5

Dbouk T (2017) A review about the engineering design of optimal heat transfer systems using topology optimization. Appl Therm Eng 112:841 – 854. https://doi.org/10.1016/j.applthermaleng.2016.10.134. http://www.sciencedirect.com/science/article/pii/S135943111632645X

Funke SW, Farrell PE (2015) A framework for automated pde-constrained optimisation. ACM Trans Math Softw 2015-Janua(212):4207–4211. https://doi.org/10.1145/0000000.0000000

Gersborg-Hansen A, Sigmund O, Haber RB (2005) Topology optimization of channel flow problems. Struct Multidiscip Optim 30(3):181–192. https://doi.org/10.1007/s00158-004-0508-7

Guest JK, Prèvost JH (2006) Topology optimization of creeping fluid flows using a darcy-stokes finite element. Int J Numer Methods Eng 66(3):461–484. https://doi.org/10.1002/nme.1560

Hess NCL, Carlson DJ, Inder JD, Jesulola E, Mcfarlane JR, Smart NA (2016) Clinically meaningful blood pressure reductions with low intensity isometric handgrip exercise. A randomized trial, vol 65, 3rd edn. CRC Press, Boca Raton. https://doi.org/10.1017/CBO9781107415324.004

Hirata SC, Couto P, Lara LG, Cotta RM (2009) Modeling and hybrid simulation of slow discharge process of adsorbed methane tanks. Int J Therm Sci 48(6):1176–1183. https://doi.org/10.1016/j.ijthermalsci.2008.09.001

Jones E, Oliphant T, Peterson P (2011) Scipy: Open source scientific tools for python. http://www.scipy.org

Karniadakis GEM, Sherwin SJ, Press OU (2005) Spectral/hp element methods for computational fluid dynamics, 2nd edn. Numerical Mathematics and Scie. OUP Oxford, Oxford

Koga AA, Lopes ECC, Villa Nova HF, Lima CRD, Silva ECN (2013) Development of heat sink device by using topology optimization. Int J Heat Mass Transfer 64:759–772. https://doi.org/10.1016/j.ijheatmasstransfer.2013.05.007

Kontoleontos EA, Papoutsis-Kiachagias EM, Zymaris AS, Papadimitriou DI, Giannakoglou KC (2012) Adjoint-based constrained topology optimization for viscous flows, including heat transfer. Eng Optim 0273(December):1–21. https://doi.org/10.1080/0305215X.2012.717074

Lazarov BS, Sigmund O (2011) Filters in topology optimization based on helmholtz-type differential equations. Int J Numer Methods Eng 86(6):765–781. https://doi.org/10.1002/nme.3072

Logg A (2007) Automating the finite element method. Arch Comput Methods Eng 14(2):93–138. https://doi.org/10.1007/s11831-007-9003-9

Matranga KR, Myers AL, Glandt ED (1992) Storage of natural-gas by adsorption on activated carbon. Chem Eng Sci 47(7):1569–1579. https://doi.org/10.1016/0009-2509(92)85005-v

Matsumori T, Kondoh T, Kawamoto A, Nomura T (2013) Topology optimization for fluid-thermal interaction problems under constant input power. Struct Multidiscip Optim 47(4):571–581. https://doi.org/10.1007/s00158-013-0887-8

Mota JPB, Rodrigues AE, Saatdjian E, Tondeur D (1996) Charge dynamics of a methane adsorption storage system: Intraparticle diffusional effects. Adsorption 3(2):117–125. https://doi.org/10.1007/BF01650235

Mota JPB, Esteves IAAC, Rostam-Abadi M (2004) Dynamic modelling of an adsorption storage tank using a hybrid approach combining computational fluid dynamics and process simulation. Comput Chem Eng 28(11):2421–2431. https://doi.org/10.1016/j.compchemeng.2004.06.004

Rahman KA, Loh WS, Chakraborty A, Saha BB, Chun WG, Ng KC (2011) Thermal enhancement of charge and discharge cycles for adsorbed natural gas storage. Appl Therm Eng 31(10):1630–1639. https://doi.org/10.1016/j.applthermaleng.2011.02.002

Sahoo PK, John M, Newalkar BL, Choudhary NV, Ayappa KG (2011) Filling characteristics for an activated carbon based adsorbed natural gas storage system. Ind Eng Chem Res 50(23):13,000–13,011. https://doi.org/10.1021/ie200241x

Sigmund O (2001) Design of multiphysics actuators using topology optimization - part i: one material structures. Comput Methods Appl Mech Eng 190(49-50):6577–6604. https://doi.org/10.1016/S0045-7825(01)00251-1

Smith DS, Alzina A, Bourret J, Nait-Ali B, Pennec F, Tessier-Doyen N, Otsu K, Matsubara H, Elser P, Gonzenbach UT (2013) Thermal conductivity of porous materials. J Mater Res 28(17):2260–2272. https://doi.org/10.1557/jmr.2013.179

Toledo M, Rojas C, Montes E, Veloso J, Sàez A (2013) Use of phase change materials on an adsorbed carbon dioxide storage system. Appl Therm Eng 51(1-2):512–519. https://doi.org/10.1016/j.applthermaleng.2012.09.034

Turteltaub S (2001) Optimal material properties for transient problems. Struct Multidiscip Optim 22(2):157–166. https://doi.org/10.1007/s001580100133

Vasiliev LL, Kanonchik LE, Babenko VA (2012) Thermal management of the adsorption-based vessel for hydrogenous gas storage. J Eng Phys Thermophys 85(5):987–996. https://doi.org/10.1007/s10891-012-0738-2

Vasiliev LL, Kanonchik LE, Rabetsky MI (2014) Thermally regulated cylinder for adsorption storage of a hydrogenous gas. Int J Heat Mass Transfer 71(2014):125–132. https://doi.org/10.1016/j.ijheatmasstransfer.2013.12.018

Yoon GH (2010) Topological design of heat dissipating structure with forced convective heat transfer. J Mech Sci Technol 24(6):1225–1233. https://doi.org/10.1007/s12206-010-0328-1

Yoon GH (2012) Topological layout design of electro-fluid-thermal-compliant actuator. Comput Methods Appl Mech Eng 209-212:28–44. https://doi.org/10.1016/j.cma.2011.11.005